Version of Record: https://www.sciencedirect.com/science/article/pii/S0025322722000949
Manuscript_e1a70c32941de903381b3d08bd37e0d9

Modeling of sediment transport in rapidly-varying flow for coastal morphological changes caused by tsunamis

Kei Yamashita[a,b,c*], Yoshiki Yamazaki[c], Yefei Bai[d,c], Tomoyuki Takahashi[e], Fumihiko Imamura[b], Kwok Fai Cheung[c]

[a] Regulatory Standard and Research Department, Nuclear Regulation Authority, Tokyo 106-8450, Japan

[b] International Research Institute of Disaster Science, Tohoku University, Sendai 980-0845, Japan

[c] Department of Ocean and Resources Engineering, University of Hawaii at Manoa, Honolulu, Hawaii 96822, USA

[d] Ocean College, Zhejiang University, Zhoushan 316021, China

[e] Faculty of Societal Safety Sciences, Kansai University, Takatsuki 569-1098, Japan

*Corresponding author. E-mail address: yamashita_kei_md8@nra.go.jp (K. Yamashita).

Abstract. Tsunamis can cause significant coastal erosion and harbor sedimentation that exacerbate the concomitant flood hazards and hamper recovery efforts. Coupling of the non-hydrostatic model NEOWAVE and the sediment transport model STM provides a tool to understand and predict these morphological changes. The non-hydrostatic model can describe flow fields associated with tsunami generation, wave dispersion as well as shock-related and separation-driven coastal processes. The sediment transport module includes non-equilibrium states under rapidly-varying flows with a variable exchange rate between bed and suspended loads. A previous flume experiment of solitary wave runup on a sandy beach provides measurements for a systematic evaluation of sediment transport driven by shock-related hydraulic processes. The extensive impacts at Rikuzentakata, Iwate, Japan and Crescent City Harbor, California, USA from the 2011 Tohoku tsunami provide pertinent case studies for model benchmarking. We utilize a self-consistent fault-slip model to define the tsunami source mechanism and field survey data to determine the characteristic grain sizes and morphological changes. The near-field modeling at Rikuzentakata gives reasonable fits with observed large-scale erosion and sedimentation associated with transition of the incoming wave into a surge and formation of a hydraulic jump in the receding flow. The non-hydrostatic module becomes instrumental in resolving tsunami waves at the far-field shore of Crescent City. The results show good agreement with local tide-gauge records as well as observed scour around coastal structures and deposition in basins resulting from separation-driven processes. While the erosion patterns in the laboratory and field cases can be explained by suspended sediment transport in the receding flow, bed load transport can be a dominant mechanism in sediment laden flows and scour around coastal structures.

© 2022 published by Elsevier. This manuscript is made available under the Elsevier user license
https://www.elsevier.com/open-access/userlicense/1.0/

Keywords: Tsunami, sediment transport, coastal morphology, non-hydrostatic flow, non-equilibrium state, rapidly-varying flow

1. Introduction

The tsunami triggered by the 2011 Tohoku earthquake (Mw 9.0) resulted in large-scale topographic changes in many coastal areas of Japan. The floodwater reached 13 m elevation and eroded 7 m of sand dunes at the shore of Rikuzentakata, Iwate (Kato et al., 2012; Udo et al., 2012; Tanaka et al., 2012). The sand dune erosion increased exposure of the backshore areas and exacerbated the flood impacts in the city. When tsunami waves of 8 m height hit Kesennuma Bay, Miyagi, a high-velocity current caused 7 m of scour in a narrow channel (Haraguchi et al., 2012; Takahashi et al., 2013). In comparison, the 1960 Chile tsunami after traveling 23 hours across the Pacific eroded the same channel by 9 m through a series of waves with 2.9 m height and ~40-min period (Takahashi et al., 1991, 2013). As tsunamis propagate over a long distance, wave dispersion associated with non-hydrostatic processes causes short-period components to lag behind. When the initial long-period components of the 1960 Chile tsunami reached Kesennuma Bay, the sand particles eroded from the narrow pass were transported and deposited further away causing more extensive erosion than what the 2011 Tohoku tsunami did. The extent of topographic changes caused by a tsunami is influenced not just by the wave height, but also by its dominant period.

The 2011 Tohoku Tsunami reached the US West Coast after traveling 9.5 hours across the Pacific Ocean. The Santa Cruz and Crescent City harbors in California were severely impacted with observed wave heights of 1.9 and 2.5 m at the respective tide gauges. While the tsunami did not cause major flood damage, extensive erosion occurred around breakwaters and channels with large amounts of sediments deposited in boat basins (Wilson et al., 2012a, 2012b). Scour near coastal structures may compromise the stability and result in their collapse (Yeh et al., 2005; Goto et al., 2011). Sediment deposition reduces the water depth at berths and channels, significantly disrupting harbor operations. Extended closure and large repair costs of harbors can delay recovery efforts from a catastrophic tsunami. Over 100 tsunamis have struck the US West Coast since 1800 (Lander et al., 1993). Crescent City Harbor has experienced disproportionate impacts in the form of erosion and sedimentation due to resonance over the continental shelf (González et al., 1995; Horrillo et al., 2008; Kowalik et al., 2008). Against this backdrop, good topographic data of the harbor before and after the 2011 tsunami are available to provide a benchmark for impact assessment (Wilson et al., 2012a).

The observed topographic changes resulted from a complex sequence of tsunami flow and sediment transport processes that can be inferred from numerical modeling. Dispersion is an important property for trans-Pacific propagation of tsunamis. Several models resort to the use of the Boussinesq-type equations for weakly dispersive tsunami waves (Horrillo et al., 2006; Kirby et al. 2013; Baba et al., 2015; Shigihara and Fujima, 2014). Yamazaki et al. (2009, 2011) alternatively adapted the depth-integrated Euler equations from Stelling and Zijlema (2003) and the shock-capturing scheme from Stelling and Duinmeijer (2003) in a model known as NEOWAVE (Non-hydrostatic Evolution of Ocean WAVEs). The dispersion relation has comparable accuracy as the Boussinesq-type equations of Peregrine (1967). The first-order governing equations facilitate two-way grid nesting for modeling of multi-scale processes, while the numerical scheme caters to abrupt transition of flow regimes associated with bores or hydraulic jumps. The model was able to reproduce ADCP and HFDR records of coastal and offshore currents generated by the 2011 Tohoku tsunami in the Hawaiian Islands (Cheung et al., 2013; Benjamin et al., 2016). A benchmark study showed such a low-order three-dimensional model is superior to high-order models based on Boussinesq-type equations in describing separation-driven currents (Lynett et al., 2017).

Tsunami flows can be rapidly varying with high energy at the coast, but most established sediment transport models cater to steady and uniform flows in open channels (e.g., Einstein, 1950; Bagnold, 1966; Itakura and Kishi, 1980; van Rijn, 1984). Empirical parameters for the vertical concentration profile (Rouse profile) and near-bed reference concentration are introduced to describe sediment transport in non-equilibrium states (van Rijn 2007; Wu and Wang, 2007). Little field evidence is available to determine whether the compatibility of these elements can be maintained for high-turbulence flows generated by tsunamis. While further research is needed in this regard, Takahashi et al. (1999) took an intermediate approach to account for non-equilibrium states under rapidly-varying flows. An exchange rate between the bed and suspended load layers was introduced in the sediment transport equations thereby integrating the uncertainties in the concentration profile and reference concentration into a single parameter. Through a series of laboratory experiments, Takahashi et al. (2000, 2011) developed a sediment transport model, known as STM (short for Sediment Transport Model), for flows similar to those of a tsunami with relatively high Shields parameters.

Coupling of STM with the non-dispersive shallow-water model TUNAMI-N2 of Imamura et al. (2006) found immediate applications in studies of topographic changes caused by massive near-field tsunamis generated by the 2004 Sumatra and 2011 Tohoku earthquakes (e.g., Ranasinghe et al., 2013; Sugawara et al., 2014a; Gusman et al., 2012; Yamashita et al., 2016, 2017). The coupled model was capable of describing qualitatively the topographic changes over wide coastal areas. These massive tsunamis produced complex flow fields with formation of vortices near the coast as well as bores and hydraulic jumps during the runup and drawdown processes. Field data show very strong currents with over 10 m/s and a Shields parameter of 10 or above (Goto et al., 2007; Paris et al., 2010). The capability to model such situations has yet to be sufficiently demonstrated and many aspects of the sediment transport process remain unknown. Accurate description of the flow field is a first step to improve modeling of sediment transport and morphological changes. By coupling NEOWAVE and STM in this study, we aim to develop a state-of-the-art tool for explaining and predicting topographic changes caused by tsunamis in both the near and far fields.

This paper describes the formulation and validation of NEOWAVE-STM and its application to investigate flow and transport processes induced by long waves through a series of case studies. Section 2 provides a summary of the governing equations and model parameters from Yamazaki et al. (2011) and Takahashi et al. (1999). Section 3 describes validation of the model capabilities with the flume experiment of Young et al. (2010) on beach profile changes caused by breaking solitary waves and subsequent rapidly-varying flows. The erosion of the sand dunes at the Rikuzentakata coast and the topographic changes in waterways and around coastal structures at Crescent City Harbor from the 2011 Tohoku tsunami provide diverse case studies to benchmark the coupled model and to investigate the transport processes pertinent to infrastructure damage. Sections 4 and 5 describe modeling of the near and far-field events as well as comparison of the computed topographic changes with survey data from Kato et al. (2012) and Wilson et al. (2012a). The laboratory and field case studies also include a parametric analysis to infer the sediment transport processes leading to the observed topographic changes and to identify uncertainties in coastal morphological modeling. Section 6 discusses the implications of this study with a summary of key findings and recommendations for future work.

2. NEOWAVE-STM

NEOWAVE and STM have been developed independently for modeling of tsunamis and sediment transport. Prior coupling of STM with TUNAMI-N2 has been based on Cartesian coordinates, which are used at the finest level of nested computational grids for inundation modeling (e.g., Ranasinghe et al., 2013; Sugawara et al., 2014a; Gusman et al., 2012; Yamashita et al., 2016, 2017). NEOWAVE utilizes spherical coordinates at all levels of computation. It is necessary to reformulate the transport equations and numerical scheme of STM into the spherical coordinate system for coupling with NEOWAVE. This section summarizes the governing equations to highlight the coupling between NEOWAVE and STM and addresses model parameters important to the laboratory and field cases considered in this study.

2.1 **Model Formulation**

NEOWAVE caters to multi-scale tsunami processes including generation at the source, propagation across the ocean as well as bore formation and inundation at the shore (Yamazaki et al., 2009, 2011). The non-hydrostatic free-surface flow is defined in a spherical coordinate system with R representing the earth radius and (λ, ϕ, z) the latitude, longitude, and altitude. Let Ω and g denote the angular velocity and gravitational acceleration; ρ_w the water density; and n the Manning's number for bottom roughness. The evolution of the flow in time t follows the continuity equation and the momentum equations in the λ, ϕ, and z-directions:

$$\frac{\partial(\zeta-\eta)}{\partial t}+\frac{1}{R\cos\phi}\frac{\partial(UD)}{\partial\lambda}+\frac{1}{R\cos\phi}\frac{\partial(V\cos\phi D)}{\partial\phi}=0 \tag{1}$$

$$\begin{aligned}&\frac{\partial U}{\partial t}+\frac{U}{R\cos\phi}\frac{\partial U}{\partial\lambda}+\frac{V}{R}\frac{\partial U}{\partial\phi}-\left(2\Omega+\frac{U}{R\cos\phi}\right)V\sin\phi\\&=-\frac{g}{R\cos\phi}\frac{\partial\zeta}{\partial\lambda}-\frac{1}{2}\frac{1}{\rho_w R\cos\phi}\frac{\partial p}{\partial\lambda}-\frac{1}{2}\frac{p}{\rho_w DR\cos\phi}\frac{\partial(\zeta-h+\eta)}{\partial\lambda}-n^2\frac{g}{D^{1/3}}\frac{U\sqrt{U^2+V^2}}{D}\end{aligned} \tag{2}$$

$$\begin{aligned}&\frac{\partial V}{\partial t}+\frac{U}{R\cos\phi}\frac{\partial V}{\partial\lambda}+\frac{V}{R}\frac{\partial V}{\partial\phi}-\left(2\Omega+\frac{U}{R\cos\phi}\right)U\sin\phi\\&=-\frac{g}{R}\frac{\partial\zeta}{\partial\lambda}-\frac{1}{2}\frac{1}{\rho_w R}\frac{\partial p}{\partial\phi}-\frac{1}{2}\frac{p}{\rho_w DR}\frac{\partial(\zeta-h+\eta)}{\partial\phi}-n^2\frac{g}{D^{1/3}}\frac{V\sqrt{U^2+V^2}}{D}\end{aligned} \tag{3}$$

$$\frac{\partial W}{\partial t}=\frac{p}{\rho_w D} \tag{4}$$

where ζ and h denote the sea-surface elevation and water depth measured from the still-water level at $z = 0$, η is the vertical seafloor displacement from $z = -h$, $D = h + \zeta - \eta$ is the flow depth, (U, V, W) represents the depth-averaged flow velocity, and p is the non-hydrostatic pressure on the seafloor at $z = -h + \eta$. The first-order governing equations utilize the non-hydrostatic pressure and vertical velocity to account for tsunami generation, wave dispersion, and flow on steep slopes. When the non-hydrostatic pressure $p = 0$, the vertical velocity in the momentum equation (4) vanishes and the governing equations (1) to (3) reduce to the nonlinear shallow-water equations.

The sediment transport model (STM) provides a macro description of grain entrainment and deposition in modifying the topography (Takahashi et al., 1999, 2000, 2011). Figure 1 illustrates the transport processes in a unit directional flow defined by the depth-averaged velocity U and flow depth D, where x is distance equal to $R\lambda\cos\phi$ and $R\phi$ along the longitude and latitude. The transport is characterized by the bed-load transport rate q_B and the depth-averaged volumetric concentration C of the suspended load in the respective layers. The net exchange from particle diffusivity and settling across the layer interface is represented by a single parameter w_{ex}. The variation of the bed load volume δv_B in time is assumed to be an order of magnitude smaller compared to other transport parameters. The transport equations for the bed and suspended loads read:

$$-\frac{\partial h}{\partial t}+\frac{1}{1-\gamma}\left\{\frac{1}{R\cos\phi}\frac{\partial q_{\mathrm{B},\lambda}}{\partial \lambda}+\frac{1}{R\cos\phi}\frac{\partial\left(q_{\mathrm{B},\phi}\cos\phi\right)}{\partial\phi}+w_{\mathrm{ex}}\right\}=0, \tag{5}$$

$$\frac{\partial CD}{\partial t}+\frac{1}{R\cos\phi}\frac{\partial\left(CUD\right)}{\partial\lambda}+\frac{1}{R\cos\phi}\frac{\partial\left(CVD\cos\phi\right)}{\partial\phi}-w_{\mathrm{ex}}=0, \tag{6}$$

where the subscripts ϕ and λ indicate transport in the respective directions and γ is the porosity of the sandy bottom. Since the bed-load layer is thin, the flow depth, instead of the thickness of the suspended load-layer, is used in the computation of the suspended transport in equation (6). The two equations are directly connected through the exchange rate w_{ex} in modifying the water depth h used in NEOWAVE.

The sediment is characterized by the specific gravity s and the grain diameter d. The settling velocity is dependent on the sediment concentration due to hindering effects and is given by Richardson and Zaki (1954) as $w_{\mathrm{s}} = w_0(1\text{-}C/C_{\mathrm{r}})^5$, where w_0 is the still-water settling velocity derived by Rubey (1933) and C_{r} is the reference concentration taken in this study to be the maximum concentration as described in Section 2.2. With reference to Figure 1, Takahashi et al. (1999) defined the bed-load transport rate q_{B} and the interlayer exchange rate w_{ex} in terms of the calibration parameters α and β as

$$\begin{aligned} q_{\mathrm{B}} &= \alpha\sqrt{(s-1)gd^3}\left(\tau_*-\tau_{*,\mathrm{c}}\right)^{1.5} && \text{if } \tau_*>\tau_{*,\mathrm{c}}, \\ &=0 && \text{if } \tau_*\le\tau_{*,\mathrm{c}}, \end{aligned} \tag{7}$$

$$\begin{aligned} w_{\mathrm{ex}} &= \beta\sqrt{(s-1)gd}\left(\tau_*-\tau_{*,\mathrm{c}}\right)^{2}-w_{\mathrm{s}}C && \text{if } \tau_*>\tau_{*,\mathrm{c}}, \\ &=-w_{\mathrm{s}}C && \text{if } \tau_*\le\tau_{*,\mathrm{c}}, \end{aligned} \tag{8}$$

where $\tau_{*,\mathrm{c}}$ is the critical Shields parameter derived by Iwagaki (1956) and $\tau_* = u_*^2/(s\text{-}1)gd$ is the non-dimensional shear stress or Shields parameter with the friction speed u_* calculated from Manning's law as $u_*^2 = gn_{\mathrm{s}}^2U|U|/D^{1/3}$. The grain roughness coefficient n_{s} differs from the Manning's number n, which accounts for the macro roughness in modeling of the flow resistance. The bed-load transport rate is influenced by the local slope. The components $q_{\mathrm{B},\lambda}$ and $q_{\mathrm{B},\phi}$ in equation (5) are augmented respectively by

$$\Delta q_{\mathrm{B},\lambda}=\left|q_{\mathrm{B},\lambda}\right|\varepsilon\frac{1}{R\cos\theta}\frac{\partial h}{\partial\lambda}, \tag{9}$$

$$\Delta q_{\mathrm{B},\phi}=\left|q_{\mathrm{B},\phi}\right|\varepsilon\frac{1}{R}\frac{\partial h}{\partial\phi}, \tag{10}$$

where ε is a diffusion coefficient (Watanabe et al., 1986). These diffusion terms become important for scour or sedimentation around a structure, where the local slope can be a limiting factor in the bed-load transport.

The governing equations for the non-hydrostatic flow and sediment transport are discretized with a staggered finite difference grid. A second-order accurate scheme integrates the continuity equation (1) for ζ at the cell center and the hydrostatic terms in the horizontal momentum equations (2) and (3) for (U, V) at the cell interface. The shock-capturing method of Stelling and Duinmeijer (2003), which is adapted with a first-order upwind scheme for improved stability, provides the advection speed for modeling bores and hydraulic jumps. The vertical momentum equation (4) is transformed into a Poisson equation from which the non-hydrostatic pressure p can be determined. The horizontal velocity (U, V) is updated from integration of the non-hydrostatic terms in the momentum equations (2) and (3) and the surface elevation ζ from the continuity equation (1). The water depth h and sediment concentration C in each cell are then determined from integration of the transport equations (5) and (6). The water depth variation is capped by a non-erodible surface, where deposition is permitted to ensure conservation of sediment volume. If the net transport out of a cell is greater than the remaining sediment volume, the out-going transport components are reduced in proportion to the remaining sediment volume to prevent erosion from penetrating the non-erodible surface. NEOWAVE and STM are weakly coupled in the present scheme, in which the fluid flow only responds to the topographic changes and vice versa. The suspended load, however, can modify the flow conditions through the fluid density and momentum transfer in a strongly coupled model (e.g., Cao et al., 2004; Xiao et al., 2010; Cantero-Chinchilla et al., 2019).

2.2 Sediment Transport Parameters

There are several grain-size dependent parameters in STM that influence the sediment transport processes. Since the basic formulation treats sand grains as having uniform size, the median diameter is used as a characteristic value in defining those parameters. Takahashi et al. (2000) determined the coefficients α and β in the transport equations (7) and (8) from a laboratory study. The uniform-flow experiments investigated the transport processes with the Shields parameter ~1 using Toyoura standard sand, which has a median diameter of about 0.2 mm. More recently, Takahashi et al. (2011) examined the dependency of α and β on grain size through a large-scale experiment with the Shields parameter ~5. Table 1 provides a summary of the results from the two series of laboratory experiments. The coefficients from Takahashi et al. (2011) can be interpolated using their values at the grain sizes of 0.166, 0.267, and 0.394 mm for general application with fine to medium sand. Following Gusman et al. (2018), an exponential function provides a suitable relationship with the grain size because α and β would gradually decrease to zero as d becomes larger. A regression analysis gives $\alpha = 9.8044\, e^{-3.366\, d}$ and $\beta = 0.0002\, e^{-6.5362\, d}$, where the unit of d is mm.

Table 1 Calibration parameters for bed load transport and exchange rates

	Takahashi et al. (2000)	Takahashi et al. (2011)		
		d = 0.166 mm	d = 0.267 mm	d = 0.394 mm
α in Eq. (7)	21.0	5.6	4.0	2.6
β in Eq. (8)	1.2×10^{-2}	7.0×10^{-5}	4.4×10^{-5}	1.6×10^{-5}

Tsunami-induced flows can have large values of the Shields parameter and the resulting sediment transport primarily occurs in the form of suspension (Takahashi et al., 2000, 2011). The sediments remain suspended in the water column due to turbulence, while the dissipation rate of turbulence energy increases with the sediment concentration. This leads to an equilibrium state wherein no further sediment supply from the bed load takes place. Sugawara et al. (2014b) assumed that tsunami flows entrain sediments as wash loads, which typically consist of finer particles with Rouse number $w_0/(\kappa u_*) < 0.8$, where κ is the von Karman constant. The energy per unit time to maintain the suspended load can be written as

$$E_r = \rho_w (s-1) g D C_s w_0 , \tag{15}$$

where C_s is the saturation concentration (van Rijn, 2007). The energy dissipation per unit time due to suspended transport is

$$E_d = e_s (\tau_m U) , \tag{16}$$

where e_s = 0.025 is the efficiency coefficient from Bagnold (1966) and $\tau_m = \rho_m u_*^2$ is the bed shear stress considering the fluid-sediment mixture density $\rho_m = \rho_w[1 + (s-1)C_s]$. The assumption of $E_r = E_d$ gives the saturation concentration

$$C_s = \frac{1}{s-1} \frac{e_s n_s^2 U^3}{D^{4/3} w_0 - e_s n_s^2 U^3} , \tag{18}$$

which depends on the grain diameter d through the still-water settling velocity w_0 and the flow conditions defined by D and U from NEOWAVE.

In sediment transport calculations, the saturation concentration of suspended sediment is applied to control grain entrainment from the bed-load layer. The sediment supply from the bed to the suspended load through the interlayer sediment exchange rate w_{ex} in Eq. (8) is not permitted if the computed concentration C is greater than the saturation concentration C_s. Super-saturation with $C \geq C_s$ can occur locally due to sediment advection, or a sudden decrease of C_s from abrupt changes in flow parameters. Settling of suspended sediments would occur gradually through w_{ex} as part of the transport process. The maximum volumetric concentration C_{max}, which is substantially higher than the saturation concentration C_s, is set to 0.377 based on the observed maximum mass concentration of 1,000 kg/m^3 by Xu (1999a, 1999b). When C

exceeds C_{max}, the excess sediments $D(C - C_{max})$ are immediately deposited to the bottom.

3. Laboratory Case Study: Flume Experiment

Young et al. (2010) conducted a large-scale flume experiment involving breaking solitary waves, bores, sheet flows, and hydraulic jumps on a sandy beach. The simple laboratory and numerical model setups allow a systematic comparison of the computed erosion and deposition processes with observations made during the experiment. The recorded beach profile change from the rapidly-varying flow provides validation of the new capabilities synergized in NEOWAVE-STM and to examine the model sensitivity to key transport parameters before its implementation to the two field cases.

3.1 Model Setup

The laboratory experiment of Young et al. (2010) was conducted in a 41.5 m long, 2.16 m wide, and 2.1 m high flume, which was installed in the Tsunami Wave Basin of 48.8 m long and 26.5 m wide at Oregon State University. Fig. 2a provides a schematic of the flume experiment and the numerical model setup. The wave maker at $x = 0$ m spans the entire 26.5 m width of the basin with a water depth of $h = 1$ m. The flume had an open end facing the wave maker and the side walls extended from $x = 3$ to 41.5 m. The incident solitary wave amplitude of $A/h = 0.6$ is the largest that can be generated in the Tsunami Wave Basin. A beach made of 70 m^3 of natural sand extended from $x = 12$ m to the end of the flume. It was built to a 1:15 slope and was not re-graded after each test. The beach profile, shown in the figure, corresponds to the conditions prior to the series of tests considered in this study. The flume was instrumented with multiple gauges and sensors to record the flow conditions and morphological changes.

The numerical model follows closely the laboratory setup. The initial beach profile from $x =$ 12 to 37 m is extended and gradually transitioned to a 1:15 slope through the end of the computational domain at $x = 57$ m. The longer flume in the numerical model provides a buffer to prevent the flow from reaching the reflective boundary at the top of the beach. The sand is well sorted with median diameter $d_{50} = 0.2$ mm, specific gravity $s = 2.65$, and porosity $\gamma = 0.4$. The Manning-Strickler formula $n = k_s^{1/6}/7.66g^{0.5}$ gives a Manning's number of $n = 0.01$ m$^{-1/3}$s for the roughness height of $k_s = 2.5d_{50}$. A radiation-type open boundary condition is applied at $x = 0$ m to mimic the setup of the flume in the Tsunami Wave Basin. The grid size and time step are set to $\Delta x = 0.125$ m and $\Delta t = 0.005$ s. An elapsed time of 150 seconds covers the runup and drawdown processes on the beach as well as a period for particle settling. Any remaining sediment from the suspended load is then forced to deposit on the bottom immediately underneath. The cumulative beach profile change from three consecutive solitary wave tests provides a direct comparison with the measurements from Young et al. (2010).

The laboratory experiment involved a large-amplitude solitary wave with energetic breaking near the water line. The shock-capturing scheme in NEOWAVE approximate wave breaking as bore formation and conserves the flow volume and momentum across the discontinuity to account for energy dissipation. A dispersive wave model might produce an overshoot of the surface elevation immediately prior to bore formation. The issue arises from the attempt of the governing equations to balance shock-related amplitude dispersion with frequency dispersion in the depth-integrated flow (Roeber et al., 2010). Local deactivation of dispersion or non-hydrostatic terms can circumvent the artifact and allow the shock-capturing scheme to approximate wave breaking without interference from high-order effects (e.g., Roeber and Cheung, 2012; Shi et al., 2012; Tonelli and Petti, 2012). Young et al. (2010) reported initiation of wave breaking at x = 22 m, where the flow transitions to flux-dominated during the runup and drawdown processes. The non-hydrostatic term is switched off in this region. The maximum Froude number is set to 4 as a limiter for the velocity in sheet flows.

3.2 Flow Field

The model results are first compared with available wave gauge and acoustic Doppler velocimeter records from the laboratory experiment. Fig. 2b shows very good agreement of the incident wave at x = 10 m in front of the beach and at x = 23, 25, 27 and 29 m, where notable transitions of the flow regime occurred. In the laboratory experiment, the solitary wave began the transformation into a plunging wave breaker at x = 22 m. The shock-capturing scheme provides a good description of the steepening wave front and decreasing amplitude from x = 23 to 25 m prior to overturning of the free surface. The computed depth-integrated velocity at x = 23 m is understandably larger than the velocimeter record, which was taken below the still water surface. The plunging jet hit the water surface at x = 26 m and generated a turbulence bore toward the beach. The model slightly overestimates its height at x = 27 m likely due to approximation of the violent flow in the splash zone as depth-integrated. The bore begins to collapse after crossing the waterline at x = 28 m onto the initially dry bed and transitions into a surge rushing up the slope. The sheet flow reaches x = 38.6 m on the beach versus 42.7 m from the computation likely due to fluid-particle flow and bed permeation, which are not considered in the model. The flow depth comparison at x = 29 m shows good agreement of the bore collapsing onto the dry bed as well as the subsequent receding flow from the drawdown process.

The receding flow generates a hydraulic jump after passing through the initial waterline at x = 28 m that in turn produces a bore propagating away from the beach. The model provides a reasonable description of these shock-related processes in the second half of the records at x = 27, 25 and 23 m albeit with minor offsets in timing and amplitude due to the complex flow structure. The bore undergoes amplitude and frequency dispersion over increasing water depth and transforms back into a solitary wave as the reflection from the beach. The computed solitary wave and its trailing super-harmonics show very good agreement with the gauge measurements at x = 10 m. The recorded negative pulse, which immediately follows in the time series, is likely a partial reflection of the outgoing solitary wave from the basin water at the open end of the flume. Such effects are not captured by the radiation condition implemented at the open boundary. This negative reflection continued to propagate toward the beach as shown by the extended time series in Young et al. (2010) and might have some influence on the beach profile that is not considered in the numerical model. Although the bore and hydraulic jump involve extensive splashing, air entrainment, and turbulence, the model provides a good description of the depth-integrated flow velocity and depth for computation of sediment transport during the most critical, initial stage of the tests.

3.3 Sediment Transport Processes

With reproduction of the rapidly-varying flows in the laboratory experiment, the observed sediment transport processes allow calibration of STM and validation of its coupling with NEOWAVE. Fig. 3a compares the recorded topographic changes with model results along the beach using the bed load and exchange rate coefficients (α, β) from the small and large-scale experiments of Takahashi et al. (2000, 2011). By and large, the transport coefficients from Takahashi et al. (2000) reproduce the patterns of deposition and erosion as well as their respective height and depth reasonably well. As the transport patterns are determined primarily by the fluid flow, the slightly shoreward extension of the computed erosion zone is due to the larger runup. The coefficients from Takahashi et al. (2011) lead to significant underestimation of the deposition height and erosion depth. The Shields parameter has an average of 4.9 over x = 20-40 m, where topographic changes are significant. One might be inclined to predict that the coefficients obtained by Takahashi et al. (2011) using a maximum Shields parameter of ~5 are more applicable than those obtained by Takahashi et al. (2000) using a maximum Shields parameter of ~1. When applied to high Shields parameters in the field, the sediment volume from the model of Takahashi et al. (2000) is significantly larger than those obtained by Takahashi et al. (2011) and other general river-bed models (e.g., Itakura and Kishi, 1980). While these sediment transport models do not include effects of breaking waves, Young et al. (2010) reported direct correlation between topographic changes with vortices triggered by breaking waves at x > 22 m. Although the strongly unsteady processes likely result in higher saturation concentration than the wash load approximation in Eq. 16 (Yamashita et al., 2018), the model of Takahashi et al. (1999) appears to provide a better approximation of the transport processes under energetic breaking waves through extrapolation to higher Shields parameters.

The saturation concentration of suspended sediments is another parameter that has profound effects on the transport processes. This is particularly true when the transport is dominated by suspended load as indicated by an average Rouse number of 0.59 over the active zone from x = 20 to 40 m. The use of the variable saturation concentration proposed by Sugawara et al. (2014b) along with the transport coefficients from Takahashi et al. (2000) provides a good description of the topographic changes. Fig. 3b illustrates the impact of using fixed values for the saturation concentration over the range considered in prior studies (Sugawara et al., 2014a; Morishita et al., 2014; Murakami et al., 2018). Fixing the saturation concentration leads to deteriorated predictions of the topographic changes. Most of the erosion is shifted from the initially dry beach to the water side, while the eroded sand is deposited further offshore. A high value of 5% extends the erosion zone onto the beach but overestimates both the erosion depth and deposition height. If the volume of sediment transport is low and the concentration is consistently below 1%, a fixed value for the saturation concentration would have little impact on topographic changes according to Takahashi et al. (2011). The use of variable saturation concentration appears to reproduce the extent and scale of erosion as well as the deposition volume in this laboratory test with a small Rouse number.

Young et al. (2010) reported the topographic changes in three phases: erosion at breaking and run-up of the incident wave, erosion by the sheet flow from the receding wave, and deposition near a hydraulic jump generated by the receding sheet flow. Fig. 4 shows the evolution of computed flow conditions, transport processes, and topographic changes along the most active portion of the beach in relation to these observations. The model approximates the breaking and dissipation of the incident solitary wave from t = 5 to 6 s as a collapsing bore with Froude numbers exceeding one behind the wave front. The flow leads to erosion through a series of processes from wave plunging at x = 26 m to the complete collapse of the bore at x = 30 m. The transport is dominated by bed load with strong sediment entrainment initially. The upward exchange rate increases drastically with the high velocity leading to over 10% of suspended concentration immediately behind the collapsing bore at t = 6 s. The high suspended concentration at the wave front is also observed in the numerical simulations of Apotsos et al. (2012) using Delft3D. The lag of the peak exchange and bed load behind the concentration spike indicates a transition to suspended transport in a non-equilibrium state. The flow reaches the maximum runup height around t = 10 s with relatively minor topographic changes from x = 30 to 40 m. The receding flow exhibits high sustained velocity and concentration from t = 14 to 18 s. A nearly zero exchange rate indicates saturation in the high-concentration sheet flow with limited sediment entrainment. The bed-load transport dominates the morphological processes producing the deep scour at x = 33 to 35 m on the beach face. Reentry of the supercritical receding flow generates a hydraulic jump that migrates from the initial waterline at x = 28 m to around x = 23 m. The abrupt reduction of flow velocity across the jump results in deposition and accumulation of the bed load at the two locations by t = 22 s. Suspended transport continues across the hydraulic jump with slight sedimentation as indicated by the negative exchange rate. The depth-integrated model does not describe the circulation immediately across the jump resulting in excess sediment accumulation locally as shown in Fig. 3a.

4. Near-field tsunami Case Study: Rikuzentakata, Iwate, Japan

The 2011 Tohoku tsunami caused extensive damage and topographic changes at Rikuzentakata, Iwate Prefecture. The LiDAR surveys before and after the tsunami allowed quantification of the erosion and deposition pattern for impact assessment (Kato et al., 2012). Fig. 5 shows the topography of the general area prior to the event. The city is located at the head of Hirota Bay on a typical ria coast in the Sanriku region and is surrounded by Kesengawa River to the west, mountain ridges to the northeast, and Furukawa Swamp and sand dunes to the south. The sand dunes of up to 3 m elevation were fortified by a concrete dike of 3 m elevation along the shore and a second one elevated to 5.5 m on an embankment to the north. The coastline is sheltered by three submerged breakwaters at 5~6 m water depth. The tsunami flushed away the majority of the sand dunes and inundated the entire city reaching the mountain slopes. This event has been evaluated by Yamashita et al. (2016) using TUNAMI-STM and is re-examined here with NEOWAVE-STM to provide a more refined description of the transport processes under rapidly-varying flows. In addition, we examine the relative contributions from the bed and suspended transport, along with interpretations from the laboratory case study, to offer new insights into the erosion of the sand dune system and to identify uncertainties in morphological modeling.

4.1. Model Settings

The inundation and sediment transport computations at Rikuzetakata require four levels of nested grids to cover an expanse of the northwest Pacific and to resolve the rugged Sanriku coastlines simultaneously. Table 2 summarizes the coverage and resolution of the telescopic grid system. The digital elevation model includes LiDAR topography and digitized nautical charts compiled by Yamashita et al. (2016). The level-1 grid covers the model region over East Japan and part of the northwest Pacific at 30" resolution, while the level-2 grid resolves the Central Tohoku coast and the near-shore wave processes at 6". The level-3 grid provides a transition to the level-4 grid at Hirota Bay, where coastal inundation and sediment transport are modeled with 0.2" resolution (approximately 6.2 m along latitude and 4.8 m along longitude). The self-consistent fault-slip model of Yamazaki et al. (2018), which can reproduce the global seismic records, geodetic and runup measurements in northeast Japan, and deep-water waveform records across the Pacific, defines the tsunami source in the nested-grid system. The dislocation extends 240 km along dip and 400 km along strike with average slip in the 40 km by 40 km subfaults reaching 22 and 37 m near the epicenter and trench. The large near-trench slip is common among published models incorporating tsunami observations and is a main factor for the devastating impacts along the Tohoku coast (Lay, 2018). Implementation of the planar fault solution of Okada (1985) provides the time history of seafloor deformation consistent with survey and geodetic data from Fujiwara et al. (2011) and Sato et al. (2011). Following the approach of Tanioka and Satake (1996), the computed vertical displacement is augmented by horizontal motion on local slopes for modeling of tsunami generation.

STM is coupled to NEOWAVE at the level-4 grid, where topographic changes can influence the flow field and vice versa. As with the previous study of Yamashita et al. (2016), the transport coefficients of Takahashi et al. (2011) derived from large-scale flume experiments are used for modeling of the real-world event. The variable saturation concentration from Sugawara et al. (2014b), which better resolves the topographic changes in the laboratory case study, is considered here. The grid is delineated into areas with erodible and non-erodible cells using land-use data prior to the tsunami. The bedrock elevation is unknown. The initial sediment layer, which is assumed to be 20 m thick, tapers off over a 25° gradient to the boundaries of non-erodible surfaces. This setting prevents discontinuous topographic changes at the boundaries between erodible and non-erodible cells to enhance the consistency of calculations. The analysis of post-tsunami deposits by Naruse et al. (2012) shows a median diameter of 0.267 mm, which corresponds closely to records of Iwate Prefecture prior to the event. In line with previous studies, the Manning's number is determined from the approach of Kotani et al. (1998) for fluid flow modeling and is assumed to be 0.03 $m^{-1/3}s$ for sediment transport calculations. The datum of the digital elevation model is Tokyo Peil, which is the mean sea level of Tokyo Bay. The tide level is set at -0.42 m, when the largest first wave struck the site, and the tsunami is modeled for an elapsed time of three hours after the earthquake.

4.2. Flow Field

The modeled tsunami matches the near-shore wave records along East Japan coasts. Fig. 6a shows, as an example, good reproduction of the observations at the South Iwate GPS 802 station immediately off Hirota Bay. The station at 204 m water depth recorded an initial tsunami wave with an impulsive peak of 6 m amplitude from the earthquake source followed by persistent oscillations of edge waves trapped on the continental shelf. The initial wave subsequently reaches 13 m elevation at the 10-m depth contour in Hirota Bay as shown in Fig. 6b. Also included are the waveforms obtained from the hydrostatic version of NEOWAVE with the same source model and by Yamashita et al. (2016) using a shallow-water model with a scaled-down version of the tsunami source developed by Satake et al. (2013). The hydrostatic and non-hydrostatic versions of NEOWAVE produce almost identical results indicating wave dispersion is not a significant factor in the large local tsunami. While the present and previous studies show different predictions of the initial drawdown, both yield similar results with respect to the highest water level and the subsequent waves.

NEOWAVE-STM becomes instrumental in capturing the rapidly-varying processes at the Rikuzentakata waterfront. Fig. 7 provides the topographic profile, water surface elevation, and Froude number along a cross-shore transect before the tsunami arrival and during the incoming flow, slack water, and receding flow (see Fig. 5 for transect alignment). The pre-arrival topographic profile includes subsidence from the earthquake rupture and shows the locations of the submerged breakwater, sand dunes, dikes, and Furukawa Swamp, which create highly localized flow and transport patterns. The incoming wave transitions to a critical flow through a collapsing bore at the shore with concomitant erosion of the crest of the dunes. The flow backs up and transitions to subcritical in front of the second dike. Overtopping of the dike generates a supercritical flow with high speed causing local scour before transiting back to sub-critical across Furukawa Swamp through a hydraulic jump. After streamlining the dune profile, the incoming flow gradually returns to subcritical reaching 13 m elevation at slack water. The receding flow is supercritical over the remaining dune causing its complete erosion. Reentry of the high-speed sheet flow generates a hydraulic jump by the shore with deposition of sediment. The submerged breakwaters trigger a localized supercritical flow with significant scour before transitioning back to subcritical through a second hydraulic jump. Except for the small-scale hydraulic jumps triggered by the second dike and the submerged breakwaters, the overall flow and morphological processes corroborate the laboratory case study but with longer spatial and time scales of an actual event.

The tsunami flooded the entire low-lying alluvial plain with 19 m runup on the mountain slopes. Fig. 8(a) shows the computed maximum water surface elevation and the inundation height markers obtained by the 2011 Tohoku Earthquake Tsunami Joint Survey Group (Mori et al., 2011). NEOWAVE-STM reproduces the inundation height near the entrance to Hirota Bay and in the inner alluvial valley relatively well. Fig. 8(b) provides a scatter plot of the observed and computed values at the markers. The present results have a geometric mean of $K = 0.99$ and a geometric standard deviation of $\kappa = 1.19$ as defined by Aida (1978), satisfying the recommendations of the Japan Society of Civil Engineers (2006). Also included in the scatter plot are the results from Yamashita et al. (2016) with similar values of $K = 0.97$ and $\kappa = 1.17$. These statistical parameters were achieved by a 20% reduction of the flow rate computed from the source model of Satake et al. (2013) at the boundary of the finest, one-way nested grid at Hirota Bay. In contrast, no local adjustments of the computed results are needed for the source model of the Yamazaki et al. (2018), demonstrating its consistency in reproducing the tsunami in the near field and across the Pacific.

4.3. Morphological changes

The Rikuzentakata waterfront sustained some of the most severe erosion along the Sanriku coast during the 2011 Tohoku tsunami. Figs. 9 shows the satellite images and digital elevation models before and after the event. The comparison suggests significant erosion of the dune and dike complex as well as the shore across Furukawa Swamp despite being covered by vegetation and pavement. NEOWAVE-STM reproduces the overall erosion pattern including distinct scour channels extending into near-shore waters. The topography and dominant wave period might have contributed to the large-scale erosion at the waterfront. As demonstrated by Yamashita et al. (2016), the reflection of the initial surge by the steep mountain slopes reaches the coast when the tsunami wave is receding. The resulting flow and transport processes can be inferred from the maximum Shields parameter and the minimum Rouse number in Fig. 10. Highly energetic flows with Shields parameters exceeding 40 occur near the sand dunes, between the submerged breakwaters, and near the river mouth. The values in these areas increase toward the ocean, corresponding to the combined flow generated by the reflected surge and receding wave. The abrupt decrease in the Shields parameter immediately off the shore corresponds to the hydraulic jump generated by the receding flow. The Rouse number is very low, at roughly 0.2, in the areas of high Shield parameters with a slight increase to 0.3 across the hydraulic jump. This suggests sediment laden water with high concentration is accompanied with the receding flow well within 30 min of the initial peak (Fig. 6). When the suspended load reaches the saturation concentration, topographic change is mainly driven by bed load, as already illustrated in the laboratory case study. A variable saturation concentration becomes important for modeling of the unsteady transport process.

Figs. 11(a) and (b) provide a comparison of the topographic changes from Kato et al. (2012) and the present study. As with the previous studies by Yamashita et al. (2016) and Arimitsu et al. (2016), NEOWAVE-STM reproduces the spatial patterns and volumes of erosion and deposition obtained by the field survey reasonably well. The model also captures detailed features such as sand dune erosion of 6~7 m deep, scour between submerged breakwaters and near river mouths as well as sediment deposits landward of the submerged breakwaters. The ~0.5 m deposit in the back-barrier Furukawa Swamp also corroborates major events inferred from paleotsunami studies (e.g., Minoura and Nakaya, 1991; Minoura et al., 1994). The erosion sites coincide with areas of large Shields parameters and low Rouse number, suggesting one-way transport of suspended sediments at high concentration over large distances. The sediment deposits landward of the submerged breakwaters are linked to the smaller Shields parameter and slightly elevated Rouse numbers from formation of the hydraulic jump. These topographic changes are direct results of the large initial wave, especially during the receding flow as illustrated in Fig. 7. The smaller subsequent waves from shelf oscillations are persistent, but play a secondary role in shaping the topography of the area. The contributions of bed and suspended transport to the topographic changes can be examined by independently reducing the coefficients α and β in equations (7) and (8) to zero. Switching the bed load off only results in localized modulation of the erosion in the central part of the dune complex as shown in Fig. 11(c). The general pattern of the erosion and deposition, which appears to be dominated by suspended transport, remains unchanged. When sand entrainment is set to zero, the sediment transport is driven only by bed load. Fig. 11(d) indicates the topographic change occurs primarily between the dunes and the submerged breakwaters with cumulative erosion and deposition of 1-2 m.

There are notable discrepancies between the observed and modeled topographic changes that highlight the uncertainties in modeling of morphological processes. The coastal dunes were protected by concrete dikes, covered by thick vegetation, and dotted with paved facilities. The model distinguishes erodible and non-erodible surfaces, but cannot account for soft protection such as vegetation and pavement. Treating the entire dune complex as bare sand leads to overestimation of the erosion. Fig. 9b shows the central portion of the vegetation, some of the paved areas, and remnants of the dikes remained after the event. The model also overestimates the depth of the scour channel at the mouth of Kesengawa River. The channel alignment corresponds well with the Shields parameter distribution associated with the outflow jet and the overestimation is likely due to the riverbed sediment size or stratification not being considered in the model. The excess sediment supply from the dunes and river provides a source for the 1~2 m of accretion seaward of the submerged breakwaters versus minor or negligible erosion from the survey. The accretion might also be a result of the breakwaters being modeled as solid structures, which interfere with the hydraulic jump formation and the transport processes. In addition, those structures were damaged by the tsunami with armor blocks scattered on the seafloor (Udo et al., 2016). The bathymetry archive and survey data, which were dated back in 1999 and May 2011, might have seasonal and other artifacts. For example, their difference infers deposition of up to 2 m of sediment on the submerged breakwaters. This is likely attributed to the lack of detailed pre-event bathymetry at and around the structures as acknowledged by Kato et al. (2012).

Table 2. Arrangement of computational grids for modeling of topographic changes at Rikuzentakata, Japan.

Region	Longitude, E	Latitude, N	#cells	$\Delta\phi$, $\Delta\lambda$	Δt	NEOWAVE	STM
1. Japan	140.3° -	35.5° -	685×	30.0"	0.5 s	Non-hydro	

	146.0°	40.6°	613				
2. Central Tohoku	141.4°- 142.2°	38.625° - 39.275°	451× 391	6.0"	0.25 s	Non-hydro	
3. Hirota Bay Vicinity	141.55° - 141.97°	38.77° - 39.13°	1261× 1081	1.2"	0.125 s	Non-hydro	
4. Hirota Bay	141.607° - 141.694°	38.948° - 39.025°	1567× 1387	0.2"	0.0625 s	Non-hydro	✓

5. Far-field tsunami case study: Crescent City Harbor, California, USA

The massive tsunami following the 2011 Tohoku earthquake traveled across the Pacific Ocean and hit the US west coast, causing over $50 million of damage to roughly 20 ports and harbors (Wilson et al., 2012a). Crescent City Harbor was one of the hardest hit with well-documented topographic changes for post-event assessment. Fig. 12 shows the harbor location in Northern California and its layout that includes a breakwater on the west, a jetty connected to a breakwater on the east, and a small boat basin with an access channel. The first wave hit the harbor approximately 9.5 hours after the earthquake. Strong currents and vortices persisted in the harbor premises for at least 3 hours causing significant scours around the breakwaters, jetty, and channel (Admire et al., 2014). Numerous boats and berthing facilities inside the basin were damaged in addition to a large amount of sediment deposition, forcing its closure for a long period of time. In addition to benchmarking NEOWAVE-STM for separation-driven flow, this case study allows investigation of morphologic changes around coastal structures and in waterways that are crucial to structural safety and harbor operation.

5.1. Model Setup

The computation utilizes five levels of two-way nested grids with increasing resolution from the Northern Pacific Ocean to Crescent City Harbor. Table 3 summarizes the coverage and resolution of the telescopic grid system. The level-1 grid at 2' resolution facilitates propagation of the tsunami from the source to the west coast of North America with optimal model dispersion in NEOWAVE (Li and Cheung, 2019). The level-2 grid resolves the continental margin at 30", while the level-3 and 4 grids provide a transition to the level-5 grid, which resolves the detailed flow and sediment processes in and around the harbor at 0.3" (approximately 9.25 and 6.9 m along the longitude and latitude). The digital elevation model in the level-5 grid, as shown in Fig. 12, includes a 2008 hydrographic survey dataset published by the National Oceanic and Atmospheric Administration (NOAA) and the 1/3" grid developed by the NOAA National Centers for Environmental Information. The pile-supported piers near the entrance to the small boat basin were manually removed and the bathymetry interpolated. As with the near-field case study in Section 4, the self-consistent source model of Yamazaki et al. (2018) defines the time history of seafloor excitation for tsunami generation. The digital elevation model references the local mean sea level. The initial water level of -0.74 m corresponds to the tides when the largest forth wave struck.

STM is coupled with NEOWAVE at the level-5 computation. The entire seafloor is modeled as an erodible layer of 20 m thick, which tapers off over a 25° gradient to non-erodible cells on land including rocky outcrops. Wilson et al. (2012a) described the tsunami deposits in the harbor area as silty sand. A uniform particle diameter of 0.1 mm is accordingly set for the sediment layer. The Manning's number assumes a standard value of 0.025 $m^{-1/3}s$ for general seafloor to describe effects of bottom friction on fluid flow and sediment transport. Since the pier structure outside the small boat basin is removed from the model grid, an equivalent roughness coefficient is implemented over the structure footprint to account for dissipation of flow energy by the piles. Based on Aburaya and Imamura (2002) and Harada and Kawata (2004), the equivalent roughness coefficient for a pile array is

$$n = \sqrt{\frac{C_{\mathrm{D}}}{2g} LND^{4/3}} \tag{19}$$

where L = 0.3 m is the pile diameter, N = 0.44/m^2 is the number of piles per unit area, and C_{D} = 1.0 is the drag coefficient, based on a typical pier design. Since the equivalent roughness coefficient is a function of the flow depth D, its value is constantly adjusted during the computation.

5.2. Flow field

The tsunami reaches the northern California coast after traveling 7500 km along the great circle path across the North Pacific Ocean. There are a number of Deep-ocean Assessment and Reporting of Tsunamis (DART) observations off the Aleutian and North America coasts that have provided validation for the modeled tsunami (Yamazaki et al., 2018). Fig. 13(a) shows the comparison of the computed waveform with the records at DART 46407, which is the nearest deep-water station to Crescent City. The computed waveform has been shifted by 6 min to account for travel time errors associated with the absence of earth elasticity and water density stratification in the model (Baba et al., 2017). The tsunami reaching the station has gone through significant amplitude and frequency dispersion along its great cycle path off the Aleutian Islands. Being away from the continental shelf, the record depicts the incident waves approaching Crescent City Harbor. A distinct leading crest of 0.15 m amplitude arrives approximately 9 hours after the earthquake and is followed by relatively moderate fluctuation of the sea surface elevation including short-period waves with small amplitude. The record shows a rapid drop of the sea surface after an elapsed time of 10.2 hours and then a sharp accent to a distinct peak 0.2 hours later. Short-period waves become a dominant feature in the time series thereafter. In stark contrast to the waveforms near the epicenter (Kawai et al., 2011), the DART data demonstrates the importance of dispersion in trans-Pacific propagation of tsunami waves.

Crescent City Harbor is susceptible to damage by tsunamis due to wave amplification over the continental margin and resonance oscillations in the harbor basin (e.g., Horrillo et al., 2008). Fig. 13(b) compares the tide gauge records and the NEOWAVE results with and without coupling with STM. While taking sediment transport into account produces slightly different results after the second wave, the topographic changes have negligible impacts on the sea surface oscillations at the tide gauge. The waveforms obtained from the two calculations are consistent with the observations despite having little resemblance to the DART record immediately offshore. Typical of a far-field tsunami, the first wave at the shore is not the largest and the subsequent arrivals are manifestations of edge waves trapped over the shelf. The computed and recorded wave amplitudes, in particular of 2.5 and 2.7 m for the largest forth wave, as well as the phase and timing show a high degree of agreement. The results suggest that NEOWAVE can account for both nonlinear and frequency dispersion of the tsunami from trans-Pacific propagation to shelf and harbor oscillations over a wide range of scales. Given the accurate reproduction of the recorded tsunami waveforms inside and outside the harbor, the model is expected to provide a reasonable description of the flow field, which drives the sediment transport to provide a rigorous assessment on the morphological processes.

5.3. Morphological changes

The configuration of Crescent City Harbor plays an important role in the tsunami flow and the subsequent morphological changes. The maximum Shields parameter and minimum Rouse number in Fig. 14 provide an insight into the complex processes. The jetty and breakwaters, which shelter the harbor from wind-generated waves, might have exacerbated the impact by accelerating the current through resonance oscillations and flow separation. The Shields parameter at the west breakwater head exceeds 80, which is much larger than what was computed for the open coast at Rikuzentakata in the near field. The current is very strong with Shields parameters over 40 across the harbor entrance between the west breakwater and the jetty, where nodes of harbor oscillation modes are located (Horrillo et al., 2008). In addition to local amplification of the current, the nodes at the entrance provide a mechanism to couple the harbor and shelf oscillations with long-lasting impacts (Yamazaki and Cheung, 2011). The strong current extends to the east breakwater head and the channel leading to the small boat basin. The Rouse number is very small along the path of strong tsunami flow suggesting dominance of suspended transport from the harbor entrance to the small boat basin. The sediment transport model of Takahashi et al. (2011) and the use of a variable saturation concentration of suspended sediments proposed by Sugawara et al. (2014b) are highly applicable to the transport processes in this case study.

Wilson et al. (2012a) described a hydrographic survey of the harbor to infer the topographic changes caused by the tsunami. Figs. 15 (a) and (b) show good agreement of the erosion and deposition patterns from the field survey and NEOWAVE-STM. The survey reveals significant erosion up to 5 and 4 m at the west and east breakwater heads versus 5.4 and 6.3 m within the same area from the model. There is also good agreement with the 2~3 m observed scour depth near the head of the jetty indicating reproduction of the locally accelerated flows and transport processes. The channel leading to the small boat basin is also subject to significant scour of 4 and 6.2 m from the survey and model. The model results remain literally the same, as shown in Fig. 15 (c), when the bed load is switched off in STM. With sediment entrainment off, the transport is consisted of bed load only and the results in Fig. 15 (d) indicate negligible topographic changes in most areas of the harbor. The parametric analysis indicates that the topographic changes are largely caused by suspended-load transport, as confirmed by the small Rouse number in Fig.14 (b). In areas with significant erosion, such as the breakwater heads and channel, the model indicates localized, net topographic changes by bed-load transport. These areas are characterized by large reversing flows associated with the flood and ebb currents. As a result, bed-load transport might produce transient topographic changes to a greater extent during the peak flow. Figs. 15 (e) and (f) plot the maximum transient erosion depth and deposition height from the bed-load component of the full calculation. The erosion and accretion patterns are mutually exclusive suggesting sediment transport by locally accelerated flows to adjacent areas. The maximum transient erosion from bed load is 1.0 m or approximately 15% of the total in the channel and increases to 1.7 and 1.2 m around the east and west breakwaters accounting for approximately 25% of the total. The bed load is a considerable component of the local scour and is an important factor when examining the stability of coastal structures and development of counter-measures for protection (e.g., Tomita et al., 2013; Kuriyama et al., 2020). Using a model capable of separating bed and suspended loads becomes increasingly important for harbors with coastal structures and channels.

The observed topographic changes at Crescent City Harbor represent accumulative effects from a series of tsunami waves in contrast to the near-field tsunami at the Rikuzentakata coast from the same source. The capability to capture wave dispersion during trans-oceanic propagation becomes an essential element in modeling of sediment transport caused by far-field tsunamis. Fig. 16 illustrates the time-dependent processes with snapshots of the flow field and suspended sediment concentration leading up to the most energetic fourth wave at the harbor. The inflow and outflow meandering through the harbor entrance, channel, and the small boat basin are in good agreement with observations from Admire et al. (2014). The areas around the breakwater heads and channel are significantly eroded by sand entrainment when the largest fourth wave recedes and generates a large vortex just outside the harbor. The channel is also eroded by each incoming wave with the sediment transported to the small boat basin most notably during the second cycle. NEOWAVE reproduces the strong ingress and egress of the flow as well as the clockwise vortex in the small boat basin reported by Admire et al. (2014). The transformation of the ingress jet into a vortex results in reduction of flow speed and settling of suspended sediment. Vortex formation, however, is dependent on the grid resolution and the model numerical scheme (Lynett et al., 2017). The three-dimensional structure of the vortex, which is not resolved by the depth-integrated model, also plays a role in the sedimentation process (Kihara et al., 2012). These uncertainties might explain the underestimation of deposition in the basin. Nevertheless, NEOWAVE-STM provides a general description of the sediment transport processes and a reasonable account of the topographic changes caused by separation-driven flows.

Table 3. Arrangement of computational grids for modeling of topographic changes at Crescent City Harbor, USA.

Region	Longitude, E	Latitude, N	#cells	$\Delta\phi$, $\Delta\lambda$	Δt	NEOWAVE	STM
1. North Pacific	135.0° - 245°	17.5° - 61.5°	3301×1321	2'	2.0 s	Non-hydro	
2. US West Coast	232.0° - 244.0°	31.0° - 50°	1441×2281	30"	1.0 s	Non-hydro	
3. Crescent City Vicinity	235.0° - 236.0°	41.1° - 42.3°	481×577	7.5"	0.5 s	Non-hydro	
4. Crescent City	235.725°- 235.9°	41.65° - 41.85°	421×481	1.5"	0.25 s	Non-hydro	
5. Crescent City Harbor	235.788333°- 235.83°	41.73° - 41.76°	501×361	0.3"	0.125 s	Non-hydro	✓

6. Discussion and Conclusions

Tsunami-induced topographic changes involve complex fluid flow and sediment transport processes with short temporal and spatial scales compared to other morphological phenomena. Numerical modeling can provide an account for the space-time sequence to improve understanding of the geological hazards. The coupling of NEOWAVE and STM matches the capabilities in modeling of rapidly-varying flows with corresponding non-equilibrium transport states through a time-dependent exchange rate between the bed and suspended loads. Implementation of NEOWAVE-STM in the laboratory case study reveals abrupt transition from bed-load to suspended transport by a collapsing bore, beach-face erosion caused by bed-load transport under high-concentration receding flows, and deposition of suspended sediments across a hydraulic jump in near-shore waters. These rapidly-varying flow and transport processes corroborate the modeled and observed morphological changes in the near-field case study demonstrating their commonality beyond the laboratory experiment and the new capabilities achieved by coupling of the two models. The far-field case study illustrates the model capabilities in describing large, localized erosion around coastal structures and deposition in a boat basin resulting from separation-driven currents. Common to the three case studies, the erosion patterns can be generally explained by suspended transport with high concentration during the most energetic receding flow. However, bed-load transport can play an important role in sediment laden flows and produce larger transient topographic changes from locally accelerated ebb and flood flows around coastal structures. The use of a variable saturation concentration complements the time-dependent exchange rate between bed and suspended loads in describing these transport processes.

Scaling of laboratory calibration to prototype conditions is always a challenge and is an inherent uncertainty in parameterization of complex physical processes for numerical modeling. The laboratory case study involves a plunging wave breaker with significant splashing, air entrainment, and turbulence that play an important role in the observed topographic changes. NEOWAVE-STM captures the processes as a bore collapsing into a high-velocity surge, but the violent flow in the experiment results in exceedingly high transport and entrainment rates. The calibration coefficients from the small-scale experiment of Takahashi et al. (2000) provide a proxy to speed up the transport process in reproducing the sediment laden flows as well as the observed deposition and erosion pattern. While this observation is made with limited data, further comparison with large-scale experiments, such as Yoshii et al. (2017, 2018) with comparable flow conditions, is necessary to substantiate the findings. Such *ad hoc* measures, however, are not necessary for modeling of transport processes associated with actual tsunami flows. Hydraulic jumps and bores might still develop at the shore, but plunging wave breakers are rarely seen even in catastrophic tsunami events. The model results are less sensitive to the entrainment rate as there is normally sufficient time to reach saturation concentration in the flow. The transport coefficients of Takahashi et al. (2011), which were derived for a range of particle sizes from large-scale flume experiments with high Shields parameters, remain a suitable choice for modeling of tsunami-induced morphological change. This is demonstrated by the good agreement between the observed topographic changes and model predictions for diverse transport processes in the near and far-field tsunami case studies.

NEOWAVE-STM provides a depth-integrated description of the non-hydrostatic flow field, which takes into account wave dispersion during trans-oceanic propagation. Dispersion is typically regarded as a high-order property of tsunami waves, but its influence on the amplitude and phase adds up across the ocean to have first-order effects, especially with coastal currents (Bai and Cheung, 2016). An accurate description of dispersion is important to resolve the waveform and the resulting flow time history for morphological modeling at far field locations. The Crescent City Harbor case study highlights this behavior by demonstrating the gradual build-up of the flow and transport to the peak during the fourth wave of the 2011 Tohoku tsunami event. The observed topographic changes represent cumulative effects from a series of tsunami waves lasting over three hours. In contrast, dispersion has little direct effect on flux-dominated sediment transport and might interfere with modeling of shock-related processes from energetic wave breaking as observed in the laboratory case study. The Rikuzentakata case study shows nearly identical waveforms in Hirota Bay from the hydrostatic and non-hydrostatic versions of NEOWAVE-STM and the observed sand dune erosion resulted primarily from the most energetic first wave of the near-field tsunami. Both NEOWAVE-STM and TUNAMI-STM provide consistent accounts of the overall erosion and deposition patterns in comparison to LiDAR observations. This suggests morphological computations based on nonlinear shallow-water models can provide more efficient solutions for studies of near-field tsunami impacts. Inclusion of the capability to model shock-related hydraulic processes will certainly increase the granularity of predicted morphological changes for forensic and countermeasures assessments.

The laboratory and field case studies undoubtedly highlight the uncertainties commonly encountered in morphological modeling. NEOWAVE and STM are weakly coupled with the flow depth being a common evolution variable. This is important for modeling of shock-related hydraulic processes as topographic changes might stabilize or trigger a transition in the flow regime. However, the absence of the account for flow permeation into dry soil, increased fluid density from particle entrainment, and pavement and vegetation coverage leads to overestimation of tsunami impacts by the model. These artifacts reduce model accuracy in post-event analysis, but the conservatism might become necessary in tsunami risk assessment. Inclusion of increased density of the fluid-sediment mixture and permeation into the initially dry sand bed, in theory, can improve the model prediction. There are also uncertainties in these high-order processes and minor perturbations in the morphological predictions can have considerable effects in impact assessment. It has been observed, for example, that erosion of sand dunes and spits, which serve as natural barriers, leads to substantial increase in inundation (Kato et al., 2007; Tehranirad et al., 2021; Yamashita et al., 2016; Sugawara, 2018). It is important to strike a balance between the increased inundation from erosion of protective barriers and the decrease brought by high-order flow processes that are not well defined in the modeling. The effects of model uncertainties in post-event or risk assessment are generally appreciable, but become a much more complex issue in studies of paleotsunami deposits (Sugawara et al., 2014c).

NEOWAVE-STM can provide quantitative predictions of the morphological changes observed in the laboratory and field case studies over a wide range of spatial and temporal scales. The trans-oceanic propagation and shock-related hydraulic processes are well resolved to provide additional details for modeling of sediment transport. There are still technical issues not fully addressed or understood in addition to the aforementioned model uncertainties. Further research is necessary to assure consistence of model results for general application in engineering design, mitigation planning, and paleotsunami research. While NEOWAVE-STM can be extended to account for multiple sediment sources and porous coastal structures, modeling of vortices generated by tsunamis in harbors is still an intense research topic with potential for improvement (Kihara, et al., 2012; Lynett et al., 2017; Kalligeris et al., 2021). Accurate prediction of separation-driven currents and the corresponding transport process is important for stability of coastal structures and assessment of maritime hazards. There are still needs for additional comparison with laboratory data to evaluate scaling of the calibration parameters from flume experiments as well as more diverse morphological case studies from catastrophic events such as the 2011 Tohoku and 2004 Sumatra tsunamis. In particular, observed sand deposits in back-barrier ponds and coastal plains from known events can serve as modern proxies to evaluate model skills in predicting deposit thickness and inferring tsunami size. Such investigations represent an important step to provide a framework for global risk evaluations through modeling of paleo-tsunami deposits.

Acknowledgments: We would like to thank Dr. Fuminori Kato, National Institute for Land and Infrastructure Management, Japan, for providing us with the bathymetry of the Rikuzentakata coast after the 2011 Tohoku tsunami; Mr. Rick Wilson, California Geological Survey, USA, for the bathymetry at Crescent City Harbor before and after the 2011 event; Prof. Daisuke Sugawara, Tohoku University, Japan, for his suggestions to improve the coupled model, and the anonymous reviewers for the constructive criticisms on the paper. Kei Yamashita, Tomoyuki Takahashi, and Fumihiko Imamura were supported by Joint Research Grant from International Research Institute of Disaster Science (IRIDeS), Tohoku University. Kei Yamashita and Fumihiko Imamura were also supported by JSPS Grant-in-Aid for Scientific Research (A) No. 17H01631, Joint Research Grant from IRIDeS, Tohoku University, and Endowed Research Division of Earthquake induced Tsunami Risk Evaluation Field (Tokio Marine). In addition, Kei Yamashita was supported by JSPS Grant-in-Aid for Young Scientists No. 19K15259. Yoshiki

Yamazaki, Yefei Bai and Kwok Fai Cheung received support from the National Oceanic and Atmospheric Administration (NOAA) Grant No. NA19NWS4670012. SOEST Contribution Number 11512.

Data Availability: The laboratory data used in Section 3 were digitized from Young et al. (2010) and Xiao et al. (2010). The recorded water elevation at GPS802 can be obtained from the Nationwide Ocean Wave information network for Ports and HArbourS, NOWPHAS (https://www.mlit.go.jp/kowan/nowphas/index_eng.html), the inundation and runup heights from the Tohoku Earthquake Tsunami Joint Survey (http://www.coastal.jp/tsunami2011/), the recorded DART buoy data from the National Data Buoy Center (http://www.ndbc.noaa.gov/), and the tide gauge data from NOAA Tides and Currents (https://tidesandcurrents.noaa.gov/). The topography of Rikuzentakata Coast is available from the Geospatial Information Authority of Japan (https://www.gsi.go.jp/ENGLISH/) and the bathymetry with 50 m resolution from the Cabinet office, Government of Japan (https://www.geospatial.jp/ckan/dataset/1976). The topography and bathymetry for Crescent City Harbor were obtained from the National Centers for Environmental Information and California Geological Survey. The modeled results in this paper are available at http://dx.doi.org/10.17632/br6ykjxmh8.1, which is an open-source online data repository hosted by Mendeley Data.

References:

Aburaya, T., Imamura, F., 2002. Proposal of a tsunami inundation simulation using combined equivalent roughness model. Proc. Coast. Eng. JSCE 49, 276–280 (in Japanese).

Admire, A.R., Dengler, L.A., Crawford, G.B., Uslu, B.U., Borrero, J.C., Greer, S.D., Wilson, R.I., 2014. Observed and modeled currents from the Tohoku-oki, Japan and other recent tsunamis in Northern California. Pure Appl. Geophys. 171, 3385-3403.

Aida, I., 1978. Reliability of a tsunami source model derived from fault parameters. J. Phys. Earth 26, 57–73.

Arimitsu, T., Matsuda, S., Murakami, Y., Shikata, T., Kawasaki, K., Mishima, T., Shimizu, R., Sugawara, D., 2016. Influence of computational parameters on accuracy of movable bed model for tsunamis. J. Jpn. Soc. Civil Eng. Ser. B2 (Coast. Eng.) 73(2), I_589–I_594 (in Japanese with an English abstract).

Apotsos, A., Gelfenbaum, G., Jaffe, B., 2011. Process-based modeling of tsunami inundation and sediment transport. J. Geophys. Res. 116, F01006.

Baba, T., Takahashi, N., Kaneda, Y., Ando, K., Matsuoka, D., Kato, T., 2015. Parallel implementation of dispersive tsunami wave modeling with a nesting algorithm for the 2011 Tohoku tsunami. Pure Appl. Geophys. 172 (12), 3455–3472.

Baba, T., Allgeyer, S., Hossen, J., Cummins, P. R., Tsushima, H., Imai, K., Yamashita, K., 2017.

Accurate numerical simulation of the far-field tsunami caused by the 2011 Tohoku earthquake, including the effects of Boussinesq dispersion, seawater density stratification, elastic loading, and gravitational potential change. Ocean Modell. 111, 46-54.

Bai, Y., Cheung, K.F., 2016. Hydrostatic versus non-hydrostatic modeling of tsunamis with implications for insular shelf and reef environments. Coast. Eng. 117, 32-43.

Bagnold, R. A., 1966. An approach to the sediment transport problem from general physics. Geological Survey Professional Paper 422-I, U.S. Geological Survey, Reston, Va.

Benjamin, L.R., Flament, P., Cheung, K.F., Luther, D.S., 2016. The 2011 Tohoku tsunami south of Oahu: high-frequency Doppler radio observations and model simulations of currents. J. Geophys. Res. Oceans. 121(2), 1133-1144.

Cantero-Chinchilla, F. N., Castro-Orgaz, O., Kham, A. A., 2018. Vertically-averaged and moment equations for flow and sediment transport. Adv. Water Resour. 132, 103387.

Cao, Z., Pender, G., Walls, S., Carling, P., 2004. Computational dam-break hydraulics over erodible sediment bed. J. Hydraul. Eng. 130(7), 589-703.

Cheung, K.F., Bai, Y., Yamazaki, Y., 2013. Surges around the Hawaiian Islands from the 2011 Tohoku tsunami. J. Geophys. Res. Oceans 118(10), 5703-5719.

Einstein, H.A., 1950. The bedload function for sediment transportation in open channel flows. Tech. Bull. 1026, U.S. Dep. of Agr., Washington, D.C.

Fujiwara, T., Kodaira, S., No, T., Kaiho, Y., Takahashi, N., Kaneda, Y., 2011. The 2011 Tohoku-Oki earthquake: Displacement reaching the trench axis. Science 334(6060), 1240.

González, F. I., Satake, K., Boss, E. F., Mofjeld, H. O., 1995. Edge wave and non-trapped modes of the 25 April 1992 Cape Mondocino tsunami. Pure Appl. Geophys. 144(3-4), 409–426.

Goto, K., Chavanich, S. A., Imamura, F., Kunthasap, P., Matsui, T., Minoura, K., Sugawara, D., Yanagisawa, H., 2007. Distribution, origin and transport process of boulders deposited by the 2004 Indian Ocean tsunami at Pakarang Cape, Thailand. Sediment. Geol. 202(4), 821–837.

Goto, K., Takahashi, J., Oie, T., Imamura, F., 2011. Remarkable bathymetric change in the nearshore zone by the 2004 Indian Ocean tsunami: Kirinda Harbor, Sri Lanka. Geomorphology 127, 107–116.

Gusman, A. R., Tanioka, Y., Takahashi, T., 2012. Numerical experiment and a case study of sediment transport simulation of the 2004 Indian Ocean tsunami in Lhok Nga, Banda Ache, Indonesia. Earth Planets Space 64, 817–827.

Gusman, A.R., Goto, T., Satake, K., Takahashi, T., Ishibe, T., 2018. Sediment transport modeling of multiple grain sizes for the 2011 Tohoku tsunami on a steep coastal valley of Numanohama, northeast Japan. Mar. Geol. 405, 77-91.

Harada, K., Kawata, Y., 2004. Study on the effect of coastal forest to tsunami reduction. Annu. Report, Disaster Prev. Res. Inst., Kyoto Univ. 47 C, 273-279.

Haraguchi, T., Takahashi, T., Hisamatsu, R., Morishita, Y., Sasak, I., 2012. A field survey of geomorphic change on Kesennuma Bay caused by the 2010 Chilean Tsunami and the 2011 Tohoku Tsunami. J. Jpn. Soc. Civil Eng. Ser. B2 (Coast. Eng.) 68(2), I_231-I_235 (in Japanese with English abstract).

Horrillo, J., Kowalik, Z., Shigihara, Y., 2006. Wave dispersion study in the Indian Ocean-Tsunami of December 26, 2004. Mar. Geod. 29(3), 149-166.

Horrillo, J., Knight, W., Kowalik, Z., 2008. Kuril Islands tsunami of November 2006: 2. Impact at Crescent City by local enhancement. J. Geophys. Res. 113, C01021.

Imamura, F., Yalciner, A.C., and Ozyurt, G., 2006. Tsunami modelling manual, UNESCO IOC International Training Course on Tsunami modelling, Tohoku University, Sendai, Japan.

Itakura, T., Kishi, T., 1980. Open channel flow with suspended sediments. J. Hydr. Div. 106(8), 1325-1343.

Iwagaki, Y., 1956. (I) Hydrodynamical study on critical tractive force. Trans. Jpn. Soc. Civil Eng. 1956(41), 1–21 (in Japanese).

Japan Society of Civil Engineers, 2006. Tsunami Assessment Method for Nuclear Power Plants in Japan. Tsunami Evaluation Subcommittee, Nuclear Civil Engineering Committee, Japan Society of Civil Engineers, 72 p.

Kalligeris, N., Kim, Y., and Lynett, P.J. 2021. Wave-induced shallow-water monopolar vortex: large-scale experiments. J. Fluid Mech. 910(A17).

Kato, F., Fukuhama, M., Fuji, H., Takagi, T., 2007. Tsunami damage estimation in consideration of beach transformation and dike failure. Sixth Int. Symp. Coast. Eng. Sci. Coast. Sediment Process,1008-1018.

Kato, F., Noguchi, K., Suwa, Y., Sakagami, T., Sato, Y., 2012. Field survey on tsunami-induced topographical change. J. Jpn. Soc. Civil Eng. Ser. B3 (Ocean Eng.) 68(2), I 174–I 179 (in Japanese with an English abstract).

Kawai, H., Sato, M., Kawaguchi, K., Seki, K., 2011. The 2011 off the Pacific Coast of Tohoku Earthquake Tsunami observed by GPS buoys. J. Jpn. Soc. Civil Eng., Ser. B2 (Coast. Eng.) 67(2), I_1291–I_1295 (in Japanese with an English abstract).

Kihara, N., Fujii, N., Matsuyama, M., 2012. Three-dimensional sediment transport processes on tsunami-induced topography changes in a harbor. Earth Planets Space 64, 787-797.

Kirby, J.T., Shi, F., Tehranirad, B., Harris, H.C., and Grilli, S.T., 2013. Dispersive tsunami waves in the ocean: Model equations and sensitivity to dispersion and Coriolis effects. Ocean Modell. 62, 39-55.

Kotani, M., Imamura, F., Shuto, N., 1998. Tsunami run-up simulation and damage estimation by using GIS. Proc. Coast. Eng. JSCE 45, 356–360 (in Japanese).

Kowalik, Z., Horrillo, J., Knight, W., Logan, T., 2008. Kuril Islands tsunami of November 2006: 1. Impact at Crescent City by distant scattering. J. Geophys. Res. 113, C01020.

Kuriyama, Y., Chida, Y., Uno, Y., Honda, K., 2020. Numerical simulation of sedimentation and erosion caused by the 2011 Tohoku Tsunami in Oarai Port, Japan. Mar. Geol. 427, 106225.

Lander, J., Lockridge, P.A., Kozuch, J., 1993. Tsunamis affecting the west coast of the United States 1806–1992. NGDC Key to Geophysical Research Documentation No. 29. USDOC/NOAA/NESDIS/NGDC, Boulder, CO, USA. 242 p.

Lay, T., 2018. A review of the rupture characteristics of the 2011 Tohoku-oki Mw 9.1 earthquake. Tectonophysics 733, 4-36.

Li, L., Cheung, K.F., 2019. Numerical dispersion in non-hydrostatic modeling of long-wave propagation. Ocean Modell. 138, 68-87.

Lynett, P.J., Gately, K., Wilson, R., Montoya, L., Arcas, D., Aytore, B., Bai, Y., Bricker, J.D., Castro, M.J., Cheung, K.F., David, C.G., Dogan, G.G., Escalante, C., González-Vida, J.M., Grilli, S.T., Heitmann, T.W., Horrillo, J., Kânoğlu, U., Kian, R., Kirby, J.T., Li , W., Macías, J., Nicolsky, D.J., Ortega, S., Pampell-Manis, A., Park, Y.S., Roeber, V., Sharghivand, N., Shelby, M., Shi, F., Tehranirad, B., Tolkova, E., Thio, H.K., Velioğlu, D., Yalçıner, A.C., Yamazaki, Y., Zaytsev, A., Zhang, Y.J., 2017. Inter-model analysis of tsunami-induced coastal current. Ocean Modell. 114, 14-32.

Minoura, K., Nakaya, S., 1991. Traces of tsunami preserved in inter-tidal lacustrine and marsh deposits: some examples from northeastern Japan. J. Geol. 99(2), 265–287.

Minoura, K., Nakaya, S., Uchida, M., 1994. Tsunami deposits in a lacustrine sequence of the Sanriku coast, northeast Japan. Sediment. Geol. 89(1-2), 25-31.

Mori, N., Takahashi, T., Yasuda, T., Yanagisawa, H., 2011. Survey of 2011 Tohoku earthquake tsunami inundation and run-up. Geophys. Res. Lett. 38, L00G14.

Morishita, Y., Takahashi, T., 2014. Accuracy improvement of movable bed model for tsunamis by applying for Kesennuma bay when the 2011 Tohoku tsunami arrived. J. Jpn. Soc. Civil Eng., Ser. B2 (Coast. Eng.) 70(2), I 491–I 495 (in Japanese with an English abstract).

Murakami, Y., Shikata, T., Tonomo, K., Sugawara, D., Hiraishi, T., 2018. Study on setting of saturation concentration of suspended sediment in numerical simulation of sediment transport associated with tsunami for off Takahama Bay. J. Jpn. Soc. Nat. Disaster Sci. 37(2), 165-176 (in Japanese with an English abstract).

Naruse, H., Arai, K., Matsumoto, D., Takahashi, H., Yamashita, S., Tanaka, G., Murayama, M., 2012. Sedimentary features observed in the tsunami deposits at Rikuzentakata City. Sediment. Geol. 282, 199–215.

Okada, Y., 1985. Surface deformation due to shear and tensile faults in a half-space. Bull.

Seismol. Soc. Am. 75(4), 1135–1154.

Paris, R., Fournier, J., Poizot, E., Etienne, S., Morin, J., Lavigne, F., Wassmer, P., 2010. Boulder and fine sediment transport and deposition by the 2004 tsunami in Lhok Nga (western Banda Aceh, Sumatra, Indonesia): A coupled offshore-onshore model. Mar. Geol. 268(1–4), 43–54.

Peregrine, D. H., 1967. Long waves on a beach. J. Fluid Mech. 27, 815-827.

Ranasinghe, D.P.L., Goto, K., Takahashi, T., Takahashi, J., Wijetunge, J.J., Nishihata, T., Imamura, F., 2013. Numerical assessment of bathymetric changes caused by the 2004 Indian Ocean tsunami at Kirinda Fishery Harbor, Sri Lanka. Coast. Eng. 81, 67-81.

Richardson, J. F., Zaki, W. N., 1954. Sedimentation and fluidization: Part I. Trans. Inst. Chem. Eng. 32, 35–50.

Roeber, V., Cheung, K.F., Kobayashi, M.H., 2010. Shock-capturing Boussinesq-type model for nearshore wave processes. Coast. Eng. 57, 407-423.

Roeber, V., Cheung, K.F., 2012. Boussinesq-type model for energetic breaking waves in fringing reef environments. Coast. Eng. 70, 1-20.

Rubey, W. W., 1993. Settling velocity of gravels, sand and silt particles. Am. J. Sci. 25, 325–338.

Satake, K., Fujii, Y., Harada, T., Namegaya, Y., 2013. Time and space distribution of coseismic slip of the 2011 Tohoku earthquake as inferred from tsunami waveform data. Bull. Seismol. Soc. Am. 103(2B), 1473–1492.

Sato, M., Ishikawa, T., Ujihara, N., Yoshida, S., Fujita, M., Mochizuki, M., Asada, A., 2011. Displacement above the hypocenter of the 2011 Tohoku-Oki earthquake. Science 332 (6036), 1395.

Shi, F., Kirby, J.T., Harris, J.C., Geiman, J.D., Grilli, S., 2012. A high-order adaptive time-stepping TVD solver for Boussinesq modeling of breaking waves and coastal inundation. Ocean Modell. 43-44, 36-51.

Shigihara, Y., Fujima, K., 2014. An adequate dispersive wave scheme for tsunami simulation. Coast. Eng. J. 56(1), 1450003-1-1450003-32.

Stelling, G.S., Zijlema, M., 2013. An accurate and efficient finite-difference algorithm for non-hydrostatic free-surface flow with application to wave propagation. Int. J. Numer. Methods Fluids 43(1), 1–23.

Stelling, G.S., Duinmeijer, S.P.A., 2003. A staggered conservative scheme for every Froude number in rapidly varied shallow water flows. Int. J. Numer. Methods Fluids 43(12), 1329-1354.

Sugawara, D., Takahashi, T., Imamura, F., 2014a. Sediment transport due to the 2011 Tohoku-oki tsunami at Sendai: Results from numerical modeling. Mar. Geol. 358, 18-37.

Sugawara, D., Naruse, H., Goto, K., 2014b. On the role of energy balance for numerical modelling of tsunami sediment transport. Abstract of the 2014 AGU Fall Meeting. San Francisco, California, USA.

Sugawara, D., Goto, K., Jaffe, B., 2014c. Numerical models of tsunami sediment transport - Current understanding and future directions. Mar. Geol. 352, 295-320.

Sugawara, D., 2018. Evolution of numerical modeling as a tool for predicting tsunami-induced morphological changes in coastal areas: A review since the 2011 Tohoku Earthquake. in: Santiago-Fandino V. et al. (eds.), The 2011 Japan Earthquake and Tsunami: Reconstruction and Restoration. Advances in Natural and Technological Hazards Research 47. Springer International Publishing AG, 451-467.

Takahashi, T., Imamura, F., Shuto, N., 1991. Study on flow and bathymetry change due to tsunami – case study in Kesennuma Bay during the 1960 Chilean tsunami. Proc. Coast. Eng. JSCE 38, 161–165 (in Japanese).

Takahashi, T., Shuto, N., Imamura, F., Asai, D., 1999. A movable bed model for tsunamis with exchange rate between bed load layer and suspended layer. Proc. Coast. Eng. JSCE 46, 606–610 (in Japanese).

Takahashi, T., Shuto, N., Imamura, F., Asai, D., 2000. Modeling sediment transport due to tsunamis with exchange rate between bed load layer and suspended load layer. Proc. 27th Int. Conf. Coast. Eng. ASCE, 1508–1519.

Takahashi, T., Kurokawa, T., Fujita, M., Shimada, H., 2011. Hydraulic experiment on sediment transport due to tsunamis with various sand grain size. J. Jpn. Soc. Civil Eng., Ser. B2 (Coast. Eng.) 67(2), I_231–I_235 (in Japanese with an English abstract).

Takahashi, T., Morishita, Y., Haraguchi, T., 2013. Bathymetry change caused by sediment transport due to Tsunamis. J. Jpn. Soc. Fluid Mech. 32(1), 15-20 (in Japanese).

Tanaka, H., Tinh, N. X., Umeda, M., Hirao, R., Pradjoko, E., Mano, A., Udo, K., 2012. Coastal and estuarine morphology changes induced by the 2011 Great East Japan Earthquake Tsunami. Coast. Eng. J. 54 (01), 1250010.

Tanioka, Y., Satake, K., 1996. Tsunami generation by horizontal displacement of ocean bottom. Geophys. Res. Lett. 23(8), 861-864.

Tehranirad, B., Kirby, J.T., Shi, F. 2021. A numerical model for tsunami-induced morphology change. Pure Appl. Geophys. 178, 5031-5059.

Tomita, T., Arikawa, T., 2013. Damage in ports due to the 2011 off the Pacific Coast of Tohoku Earthquake Tsunami. J. Disaster Res. 8(4), 594-604.

Tonelli, M., Petti, M., 2012. Shock-capturing Boussinesq model for irregular wave propagation. Coast. Eng. 61, 8-19.

Udo, K., Sugawara, D., Tanaka, H., Imai, K., Mano, A., 2012. Impact of the 2011 Tohoku earthquake and tsunami on beach morphology along the northern Sendai coast. Coast. Eng. J. 54, 1250009.

Udo, K., Takeda, Y., Tanaka, H., 2016. Coastal morphology change before and after 2011 off the Pacific Coast of Tohoku Earthquake Tsunami at Rikuzen-Takata Coast. Coast. Eng. J. 58(4), 1640016.

Van Rijn, L. C., 1984. Sediment transport: Part II: Suspended load transport. J. Hydraul. Eng. 110(11), 1613–1641.

Van Rijn, L. C., 2007. Unified view of sediment transport by currents and waves. II: Suspended transport. J. Hydraul. Eng. 133(6), 668–689.

Watanabe, A., Maruyama, Y., Shimizu, T., Sakakiyama, T., 1986. Numerical prediction model of three-dimensional beach deformation around a structure, Coast. Eng. Jpn. 29 (1986), 179-194.

Wilson, R., Davenport, C., Jaffe, B., 2012a. Sediment scour and deposition within harbors in California (USA), caused by the March 11, 2011 Tohoku-oki tsunami. Sediment. Geol. 282, 228-240.

Wilson, R., Admire, A. R., Borrero, J. C., Dengler, L., A., Legg, M. R., Lynett, P., McCrink, T, P., Miller, K. M., Ritchile, A., Sterling, K., Whitmore, P. M., 2012b. Observations and Impacts from the 2010 Chilean and 2011 Japanese Tsunamis in California (USA). Pure Appl. Geophys. 170(6-8), 1127-1147.

Wu, W., Wang, S.S., 2007. One-dimensional modeling of dam-break flow over movable beds. J. Hydraul. Eng. 133 (1), 48–58.

Xiao, H., Young, Y.L., Prevost, J.H., 2010. Hydro- and morpho-dynamic modeling of breaking solitary waves over a fine sand beach. Part II: Numerical simulation. Mar. Geol. 269, 119-131.

Xu, J., 1999a. Grain-size characteristics of suspended sediment in the Yellow River, China. Catena 38, 243–263.

Xu, J., 1999b. Erosion caused by hyperconcentrated flow on the Loess Plateau of China. Catena 36, 1–19.

Yamashita, K., Sugawara, D., Takahashi, T., Imamura, F., Saito, Y., Imato, Y., Kai, T., Uehara, H., 2016. Numerical simulation of large-scale sediment transport caused by the 2011 Tohoku Earthquake Tsunami in Hirota Bay, Southern Sanriku Coast. Coast. Eng. J. 58, 1640015.

Yamashita, K., Shigihara, Y., Sugawara, D., Arikawa, T., Takahashi, T., Imamura, F., 2017. Effect of sediment transport on tsunami hazard and building damage – an integrated simulation of tsunami inundation, sediment transport and drifting vessels in Kesennuma City, Miyagi Prefecture during the Great East Japan Earthquake. J. Jpn. Soc. Civil Eng.,

Ser. B2 (Coast. Eng.) 73(2), I_355–I_360 (in Japanese with an English abstract).
Yamashita, K., Sugawara, D., Arikawa, T., Shigihara, Y., Takahashi, T., Imamura, F., 2018. Improvement of tsunami-induced sediment transport model by considering saturated concentration in suspension with strong unsteady flows. J. Jpn. Soc. Civil Eng., Ser. B2 (Coast. Eng.) 74(2), I_325–I_330 (in Japanese with an English abstract).
Yamazaki, Y., Cheung, K.F., 2011. Shelf resonance and impact of near-field tsunami generated by the 2010 Chile earthquake. Geophys. Res. Lett. 38(12), https://doi.org/10.1029/2011GL047508.
Yamazaki, Y., Kowalik, Z., Cheung, K.F., 2009. Depth-integrated, non-hydrostatic model for wave breaking and runup. Int. J. Numer. Methods Fluids 61(5), 473–497.
Yamazaki, Y., Cheung, K.F., Kowalik, Z., 2011. Depth-integrated, non-hydrostatic model with grid nesting for tsunami generation, propagation, and run-up. Int. J. Numer. Methods Fluids 67, 2081–2107.
Yamazaki, Y., Cheung, K. F., Lay, T., 2018. A self-consistent fault slip model for the 2011 Tohoku Earthquake and Tsunami. J. Geophys. Res. Solid Earth 123(2), 1435-1458.
Yeh, H., Robertson, I., Preuss, J., 2005. Development of design guidelines for structures that serve as tsunami vertical evacuation sites. Technical report, Washington State Department of Natural Resources, Division of Geology and Earth Resources, Olympia, Washington.
Yoshii, T., Tanaka, S., Matsuyama, M. 2017. Tsunami deposits in a super-large wave flume. Mar. Geol. 391, 98-107.
Yoshii, T., Tanaka, S., Matsuyama, M. 2018. Tsunami inundation, sediment transport, and deposition process of tsunami deposits on coastal lowland inferred from the Tsunami Sand Transport Laboratory Experiment (TSTLE). Mar. Geol. 400, 107-118.
Young, Y.L., Xiao, H., Maddux, T., 2010. Hydro- and morpho-dynamic modeling of breaking solitary waves over a fine sand beach. Part I: Experimental study. Mar. Geol. 269, 107-118.

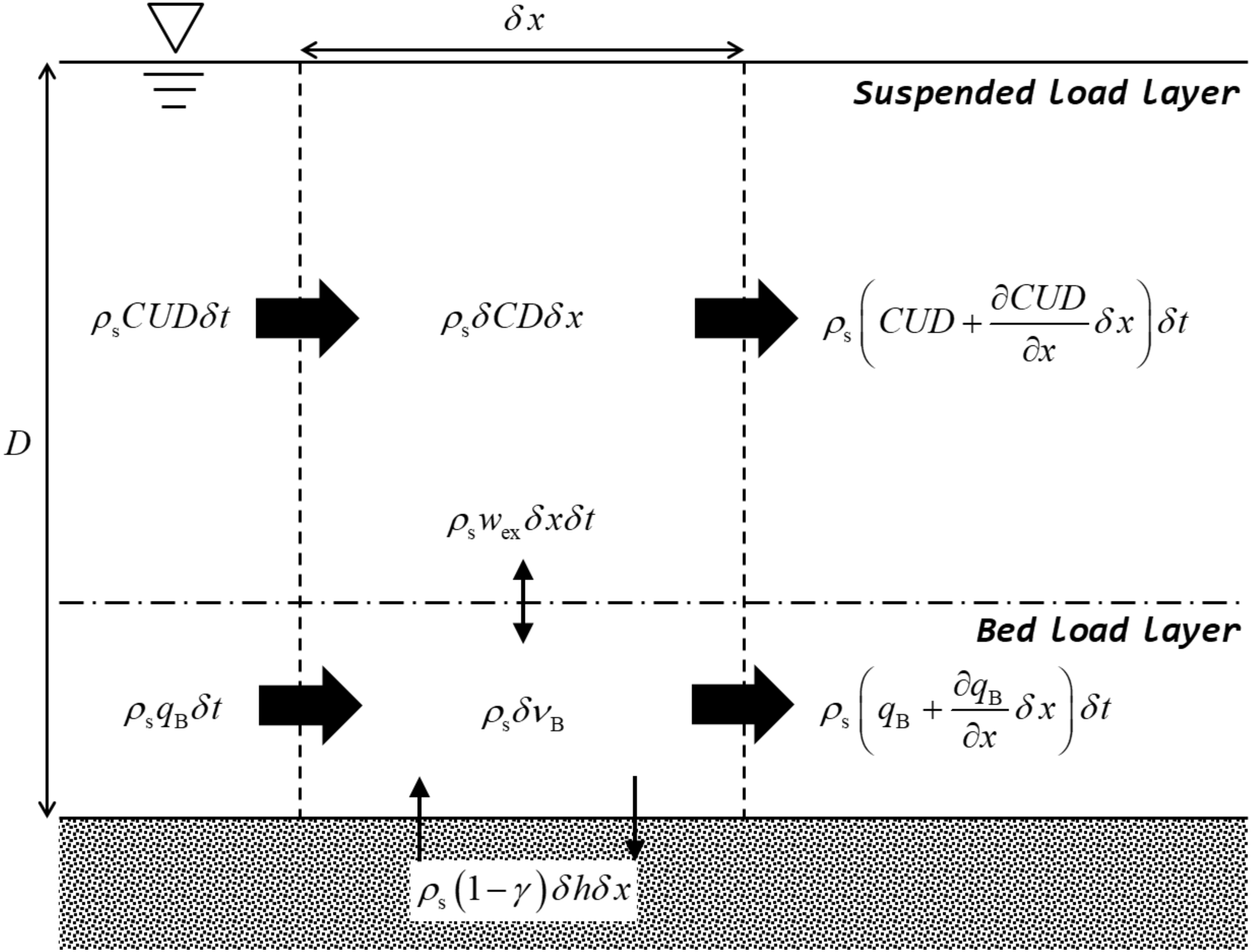

Fig. 1 Schematic of STM adapted from Takahashi et al. (1999) for coupling with NEOWAVE to model coastal morphological change caused by tsunamis.

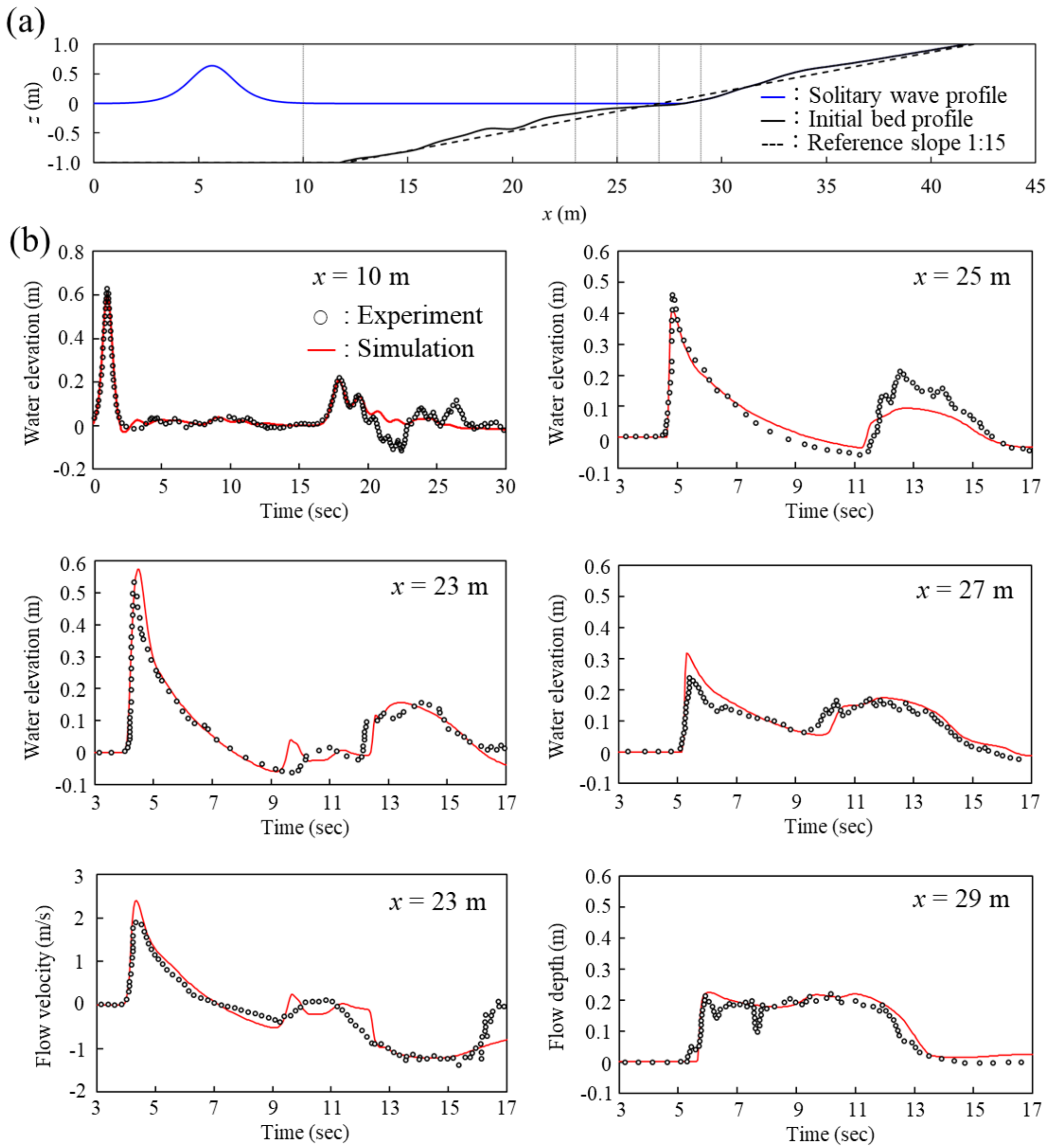

Fig. 2 Schematic of the flume experiment adapted from Young et al. (2010) and illustration of rapidly-varying flows involving shock-related hydraulic processes. (a) Initial conditions with instrument locations indicated by gray vertical lines. (b) Time series of computed and recorded flow parameters showing incident and reflected waves at x = 10 m, bore attenuation and hydraulic jump formation at x = 23, 25, 27 m; and bore collapse and receding flow at x = 29 m.

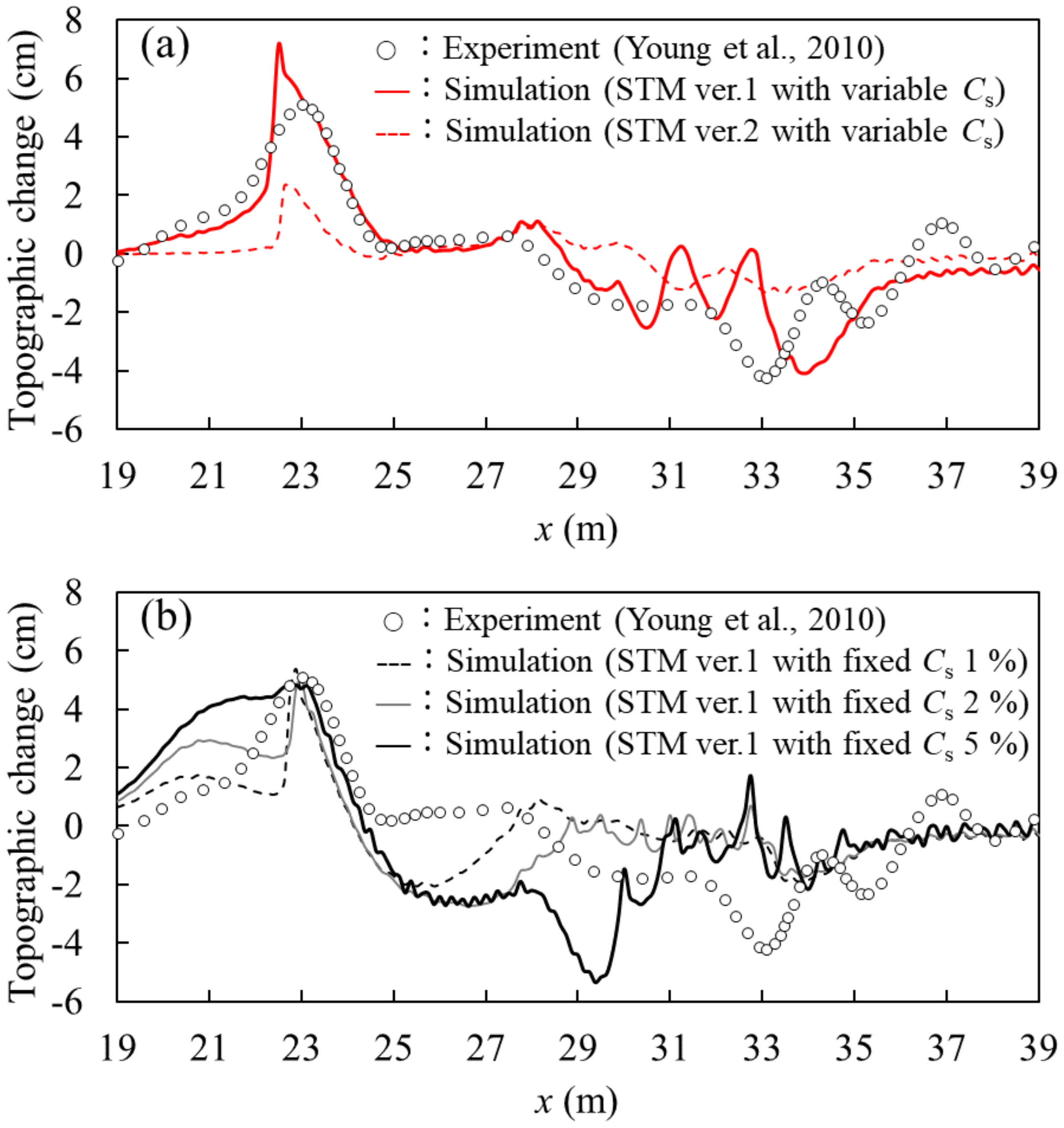

Fig. 3 Sensitivity of computed topographic changes with model parameters in relation to recorded data along the active beach segment in the flume experiment of Young et al. (2010). (a) Variable saturation concentration with calibration coefficients (α, β) from small and large-scale experiments of Takahashi et al. (2000, 2011). (b) Fixed saturation concentration with calibration coefficients from small-scale experiments of Takahashi et al. (2000).

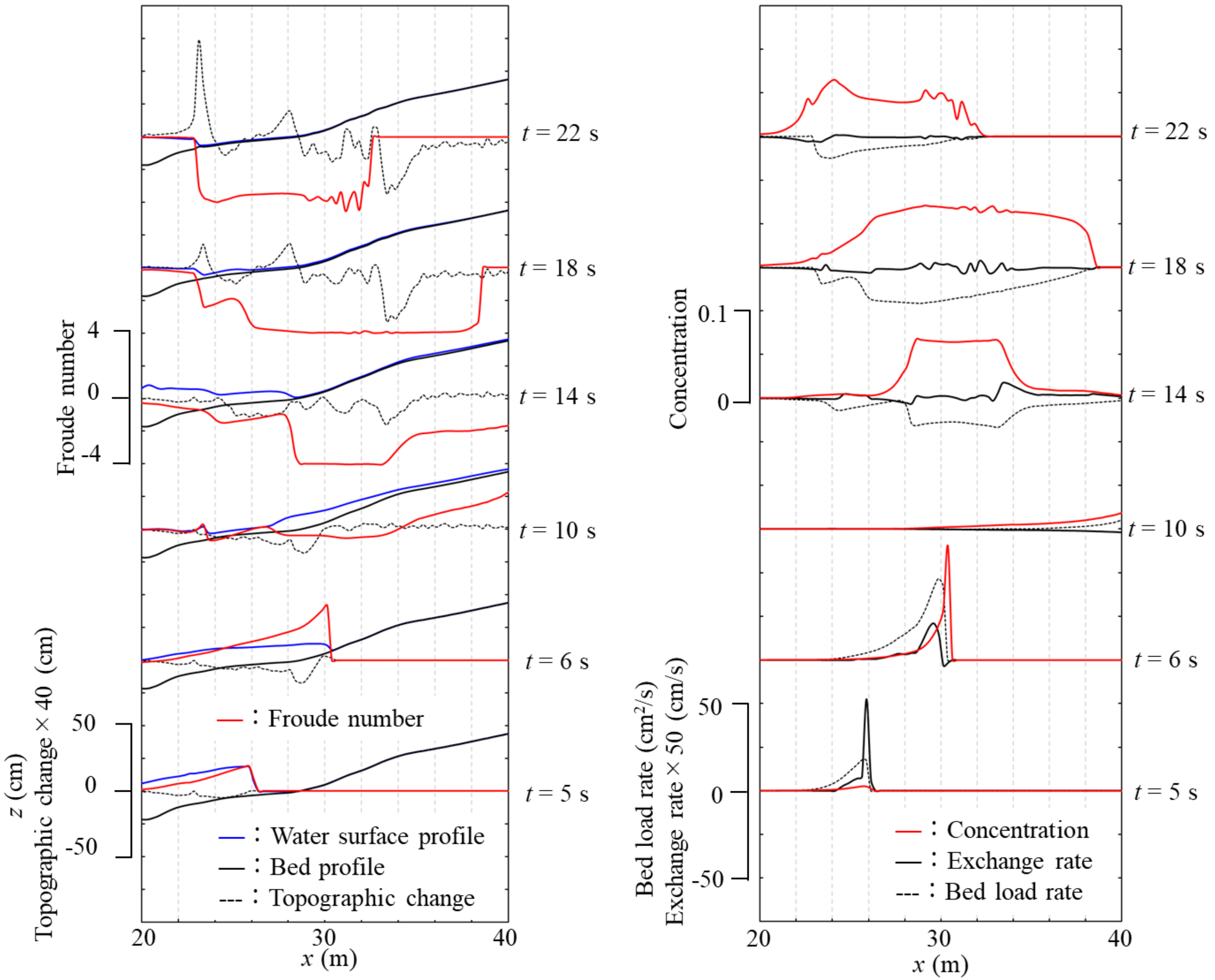

Fig. 4 Time history of computed hydrodynamic and morphological parameters along the active beach segment in the flume experiment of Young et al. (2010). Snapshots of bore formation and collapse at t = 5 and 6 s, runup at t = 10 s, offshore migration of hydraulic jump forced by receding flow from t = 14 to 18 s, and offshore hydraulic jump and sand deposition at t = 22 s.

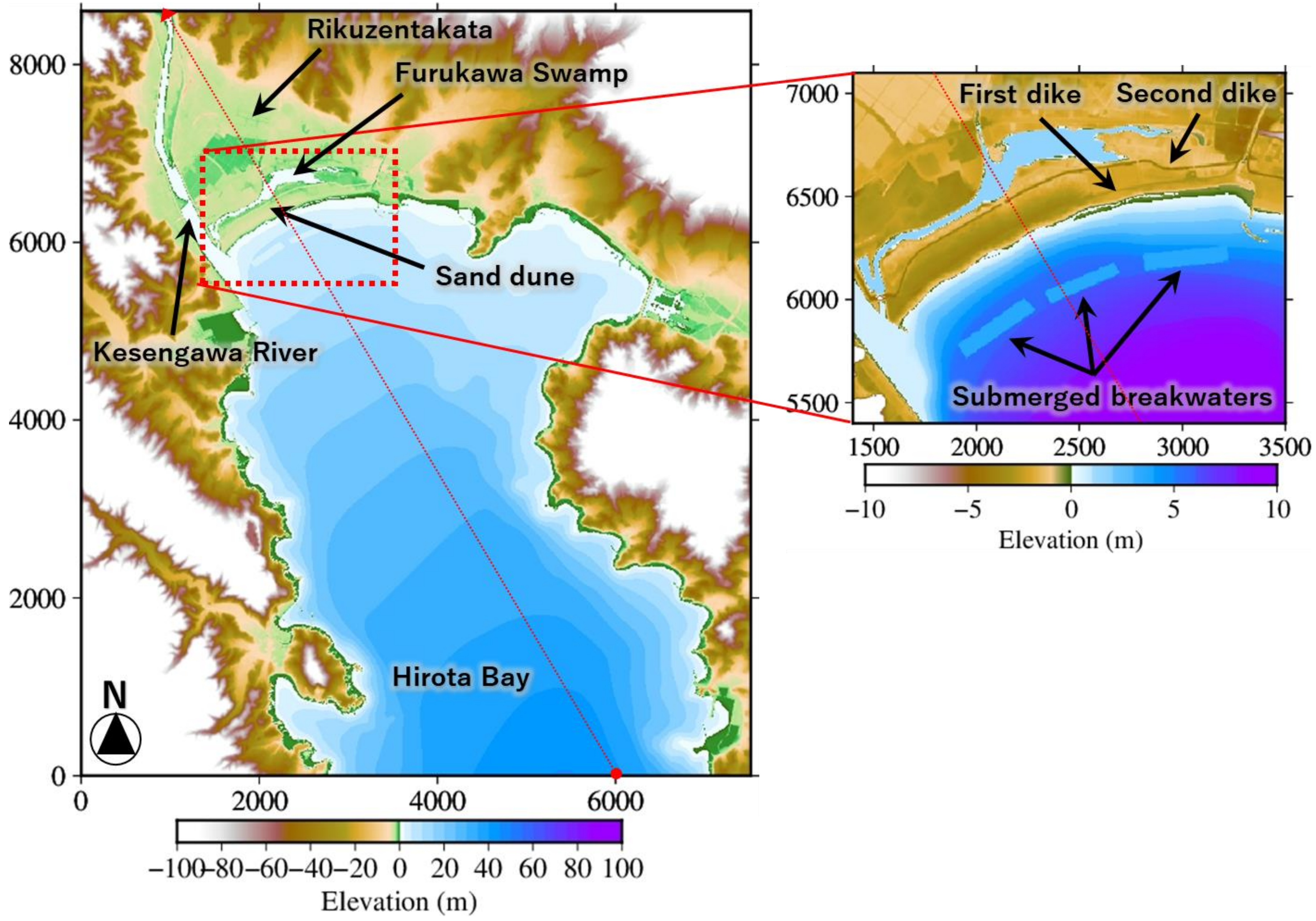

Fig. 5 Digital elevation model in the level-4 grid at Hirota Bay, Japan and close-up view of the waterfront area with key geographic features and a transect (dotted red line) for detailed analysis. The axes indicate horizontal distance in meter.

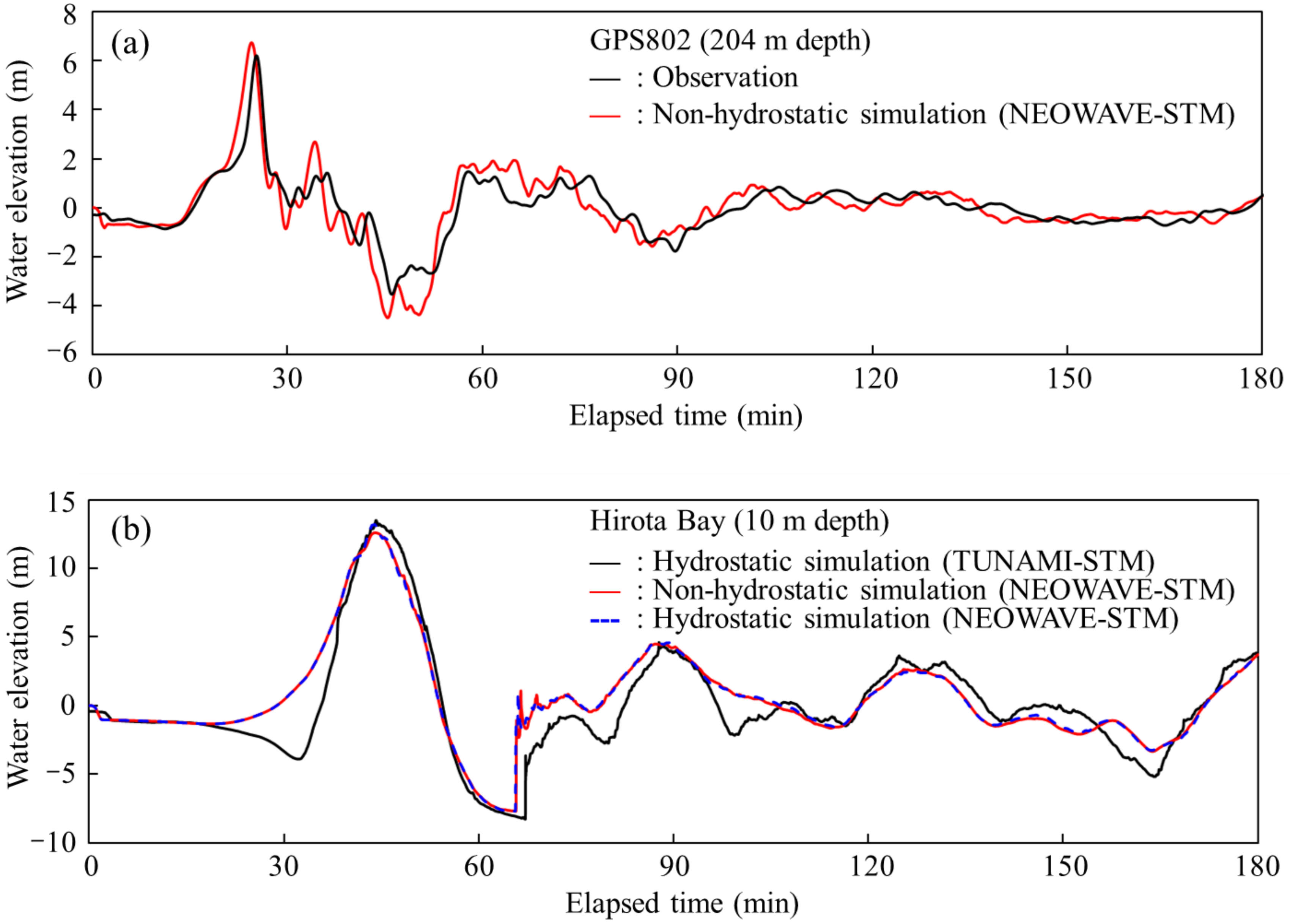

Fig. 6 Time histories of water surface elevations at Hirota Bay, Japan. (a) Non-hydrostatic model results and records at South Iwate GPS 802. (b) Hydrostatic and non-hydrostatic model results at 10 m water depth in front of the waterfront area.

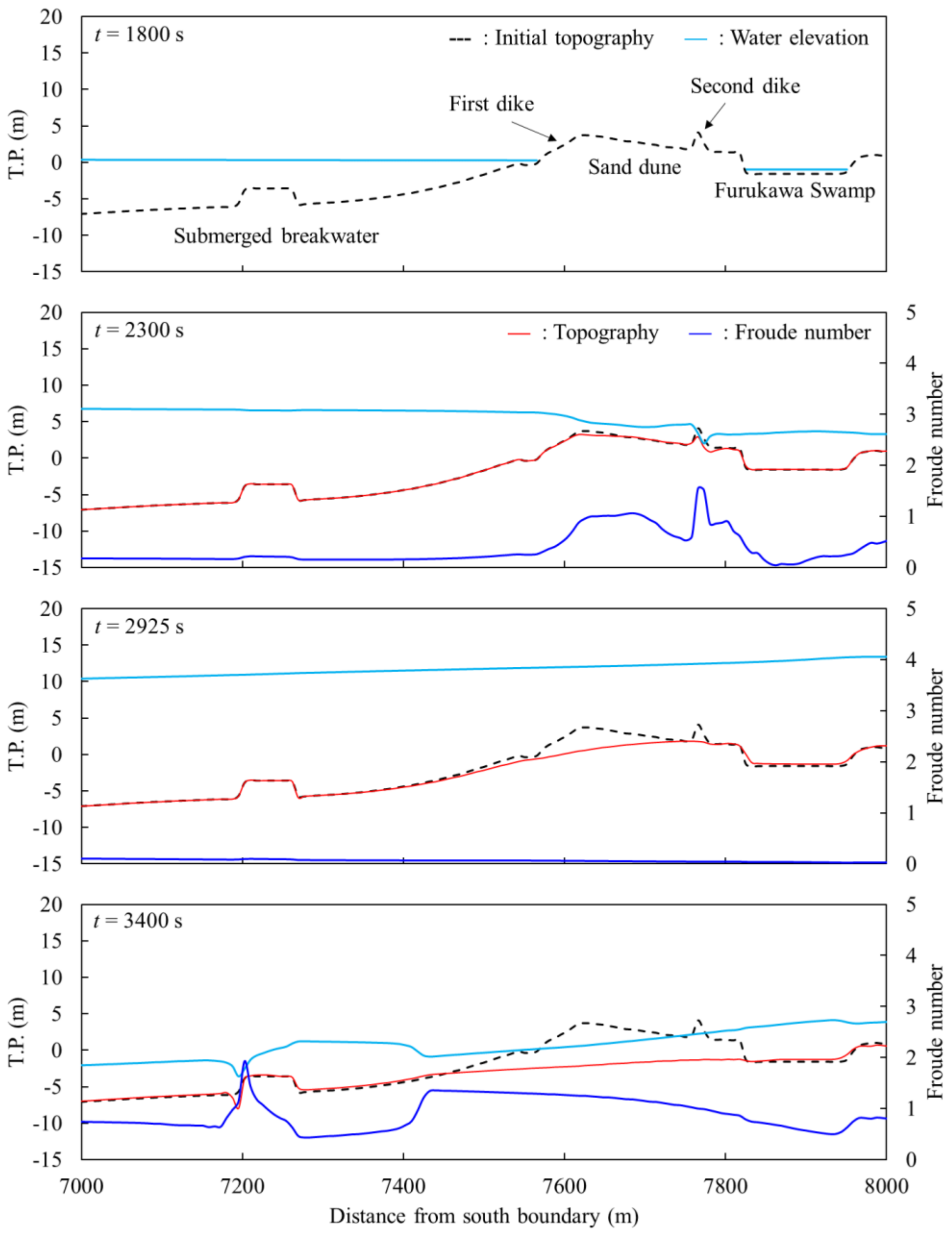

Fig. 7 Computed water surface elevation, Froude number, and topography along transect in Hirota Bay, Japan (see figure 5 for alignment). Snapshots of pre-arrival conditions with key topographic features at t = 1800 s, incoming flow at t = 2300 s, slack water at t = 2925 s, and receding flow at t = 3400 s.

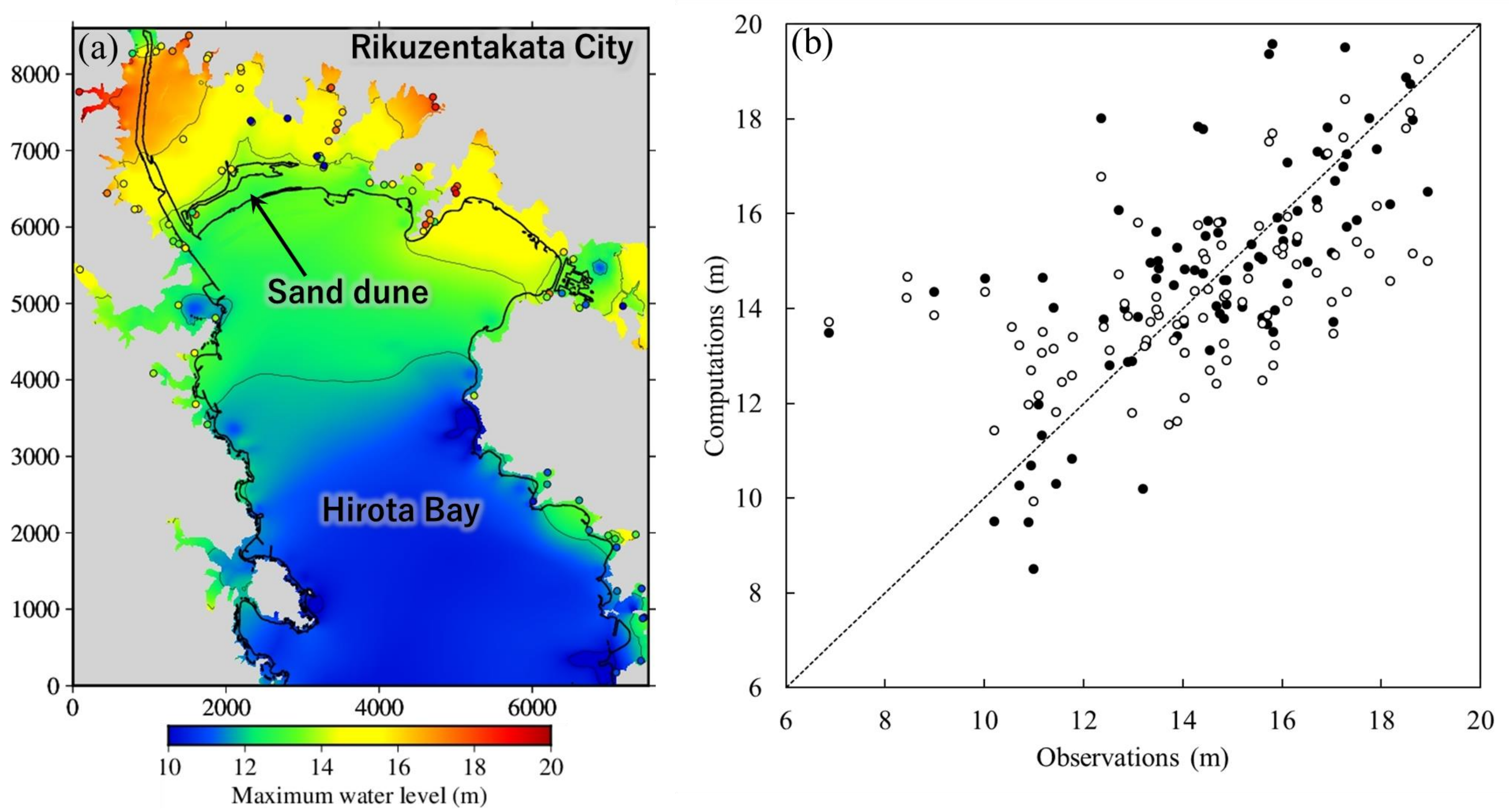

Fig. 8 Comparison of computed maximum water elevations and recorded inundation heights from Mori et al. (2011) at Rikuzentakata City, Japan. (a) Spatial distribution within the level-4 grid, where axes indicate horizontal distance in meter. (b) Scatter plot of computations versus observations. White and black circles denote results from the present study and Yamashita et al. (2016).

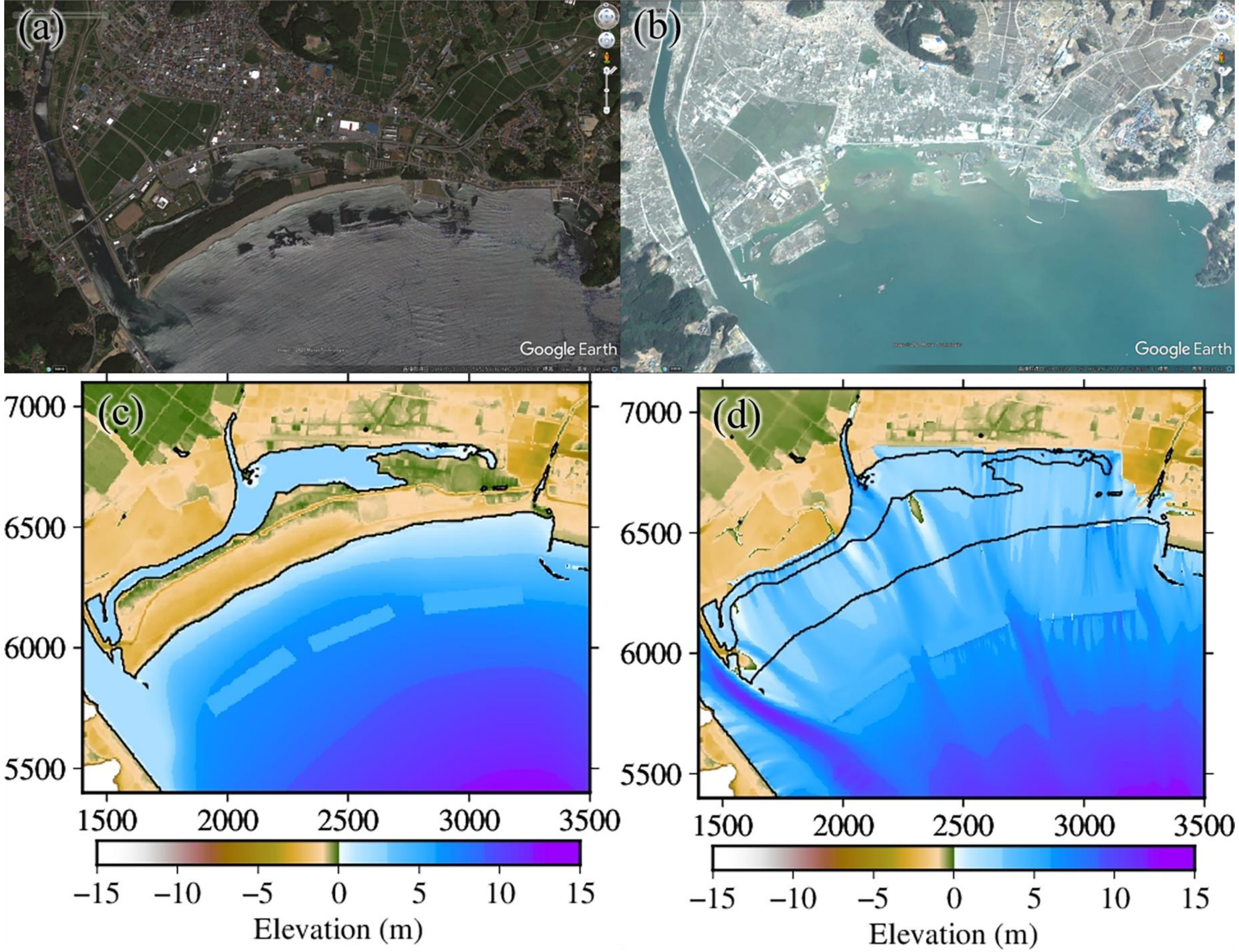

Fig. 9 Waterfront area of Rikuzentakata, Japan before and after the 2011 Tohoku tsunami. (a) Satellite image taken on 13 July 2010. (b) Satellite image taken on 14 March 2011. Both images from Google Earth cover a region of 4 km by 2.5 km. (c) Initial digital elevation model. (d) Simulated topography after the tsunami. The axes indicate horizontal distance in meter within the level-4 grid.

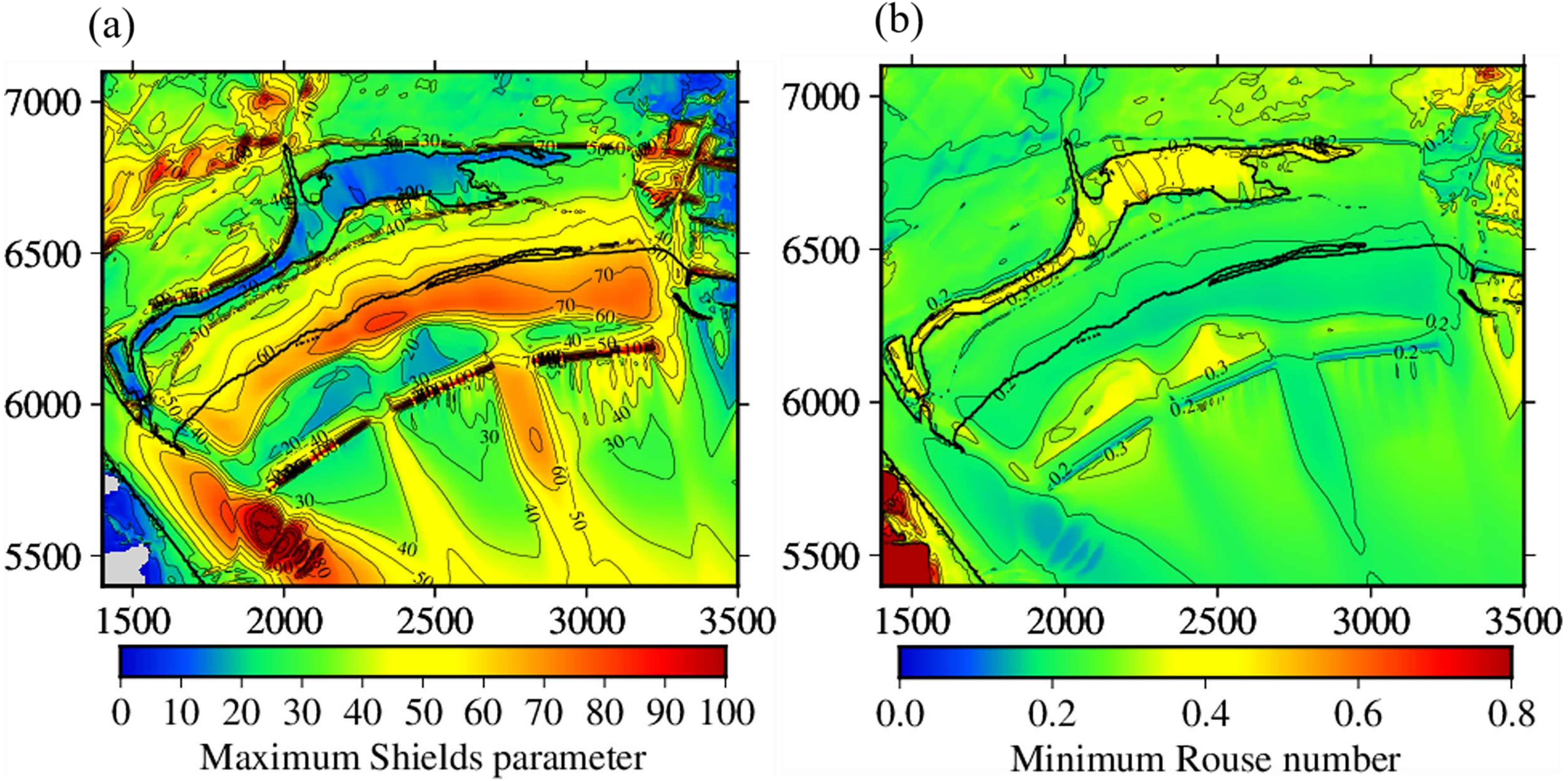

Fig. 10 Spatial distribution of sediment mobility from the 2011 Tohoku tsunami at the waterfront area of Rikuzentakata, Japan. (a) Maximum Shields parameter. (b) Minimum Rouse number. The axes indicate horizontal distance in meter within the level-4 grid.

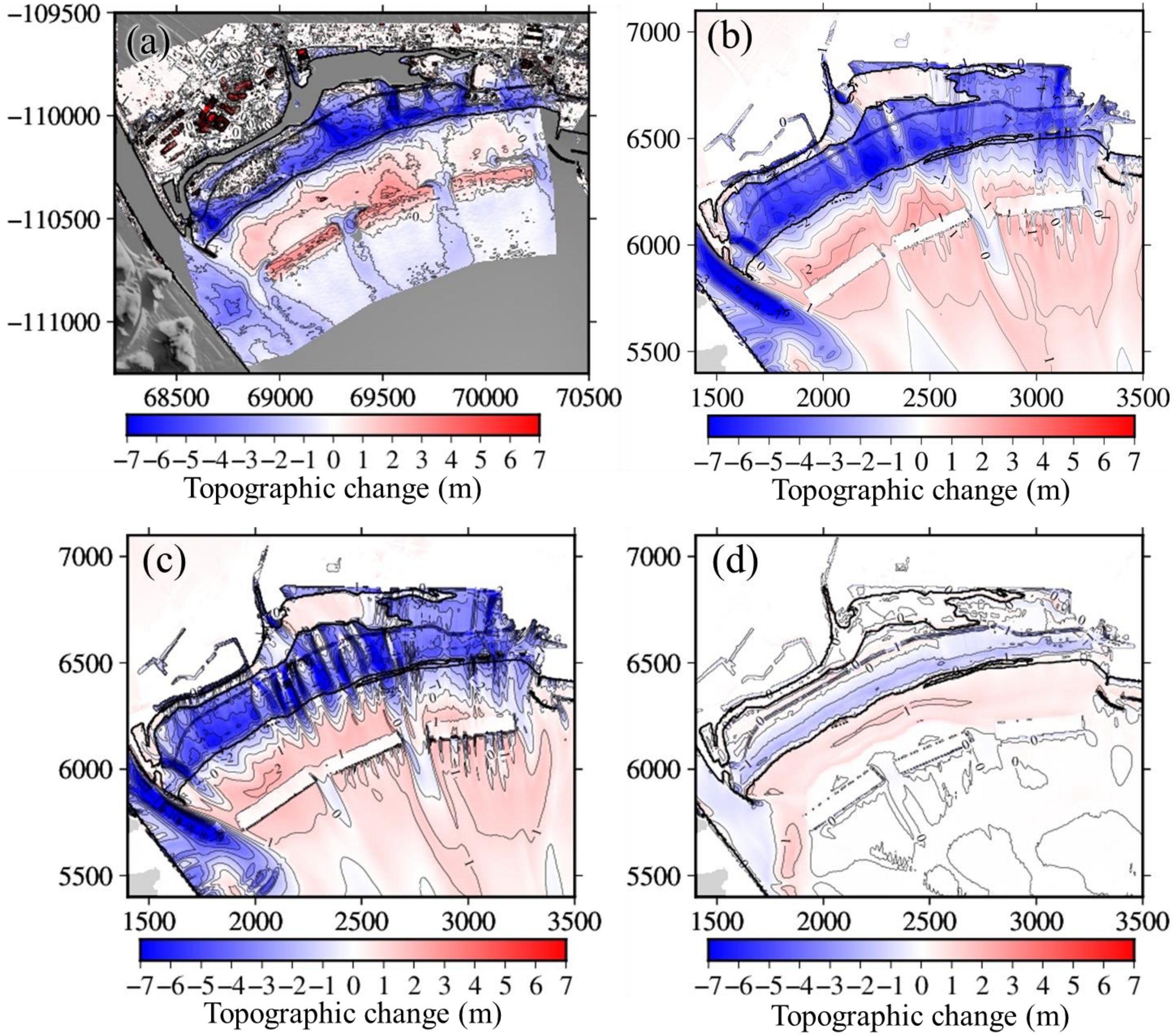

Fig. 11 Comparison of topographic changes from the 2011 Tohoku tsunami at the waterfront area of Rikuzentakata, Japan. (a) Survey results from Kato et al. (2012). The axes indicate horizontal distance in meter within the X-system of the plane rectangular coordinate system of Japan. (b) NEOWAVE-STM. (c) NEOWAVE-STM with zero bed load. (d) NEOWAVE-STM with zero sand entrainment. The axes indicate horizontal distance in meter within the level-4 grid.

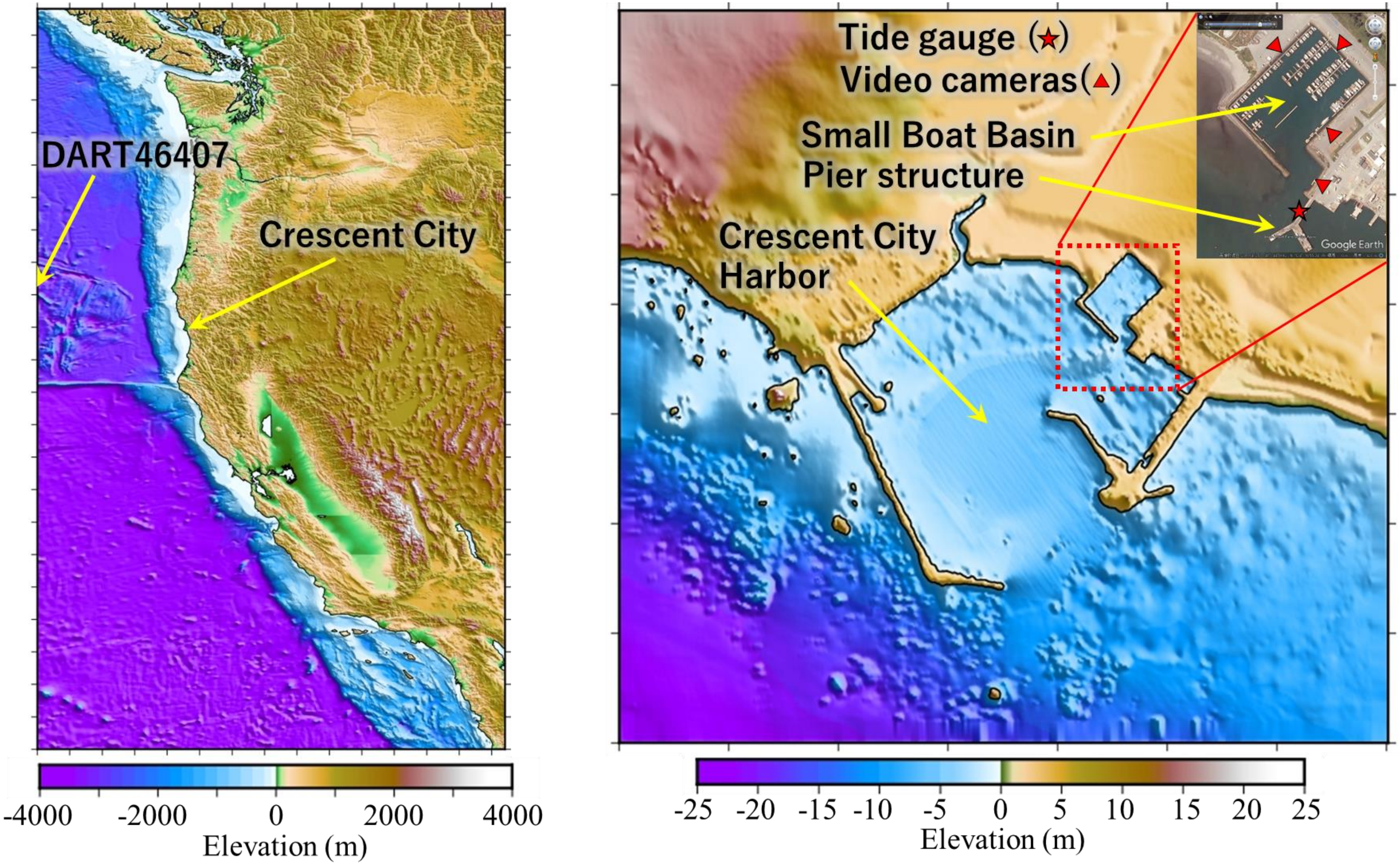

Fig. 12 Digital elevation model in the level-2 and 5 grids for the far-field case study at Crescent City Harbor, USA and location maps for key geographic features and instruments, where satellite image in right panel was obtained from Google Earth (axis grid spacing corresponds to 50' and 500 m in the left and right panels).

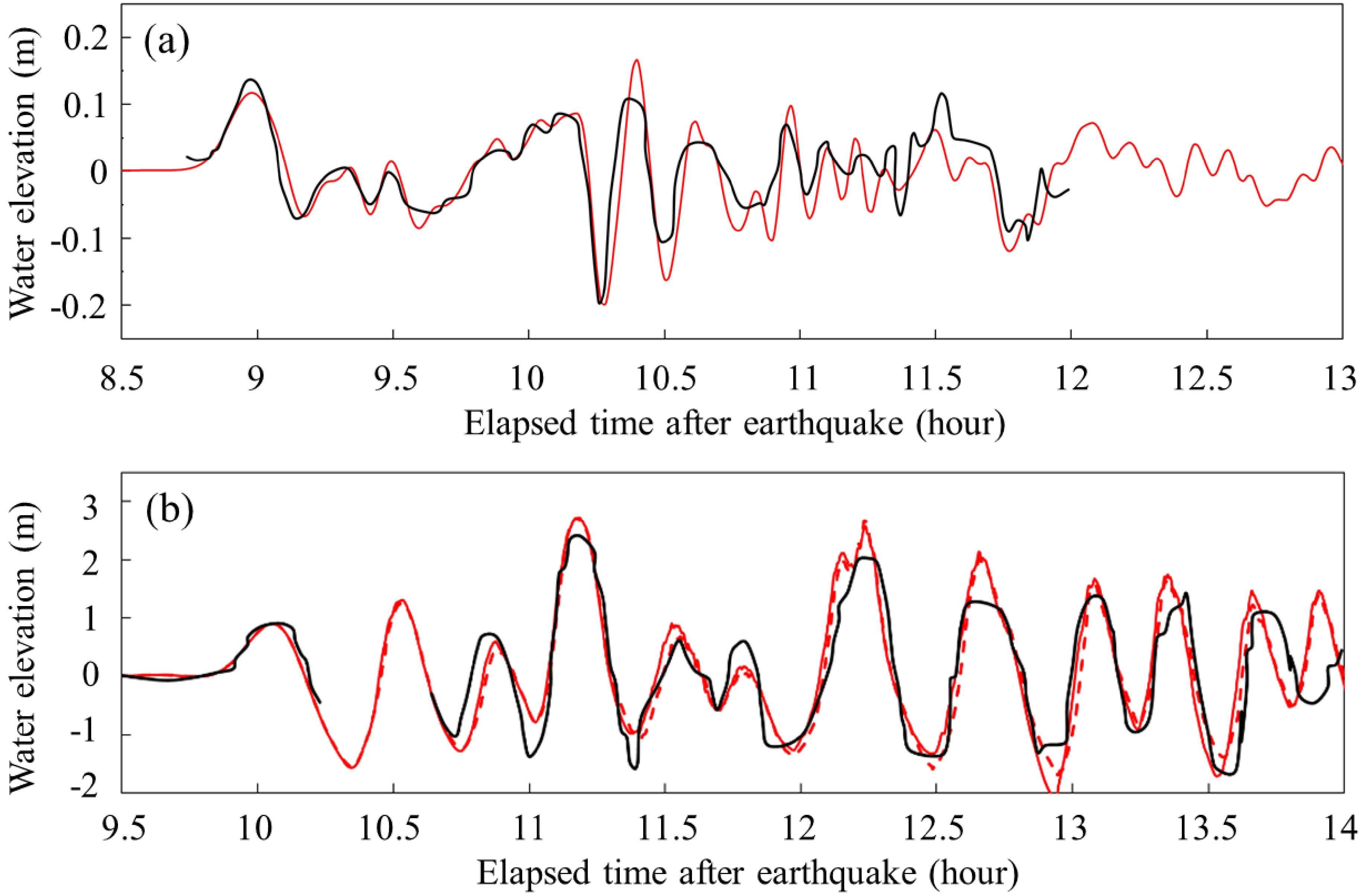

Fig. 13 Time series of computed and observed water surface elevation for the 2011 Tohoku tsunami. (a) DART 46407. (b) Tide gauge in Crescent City Harbor, USA. Black line indicates observations and solid and dashed red line denotes NEOWAVE results with and without coupling with STM.

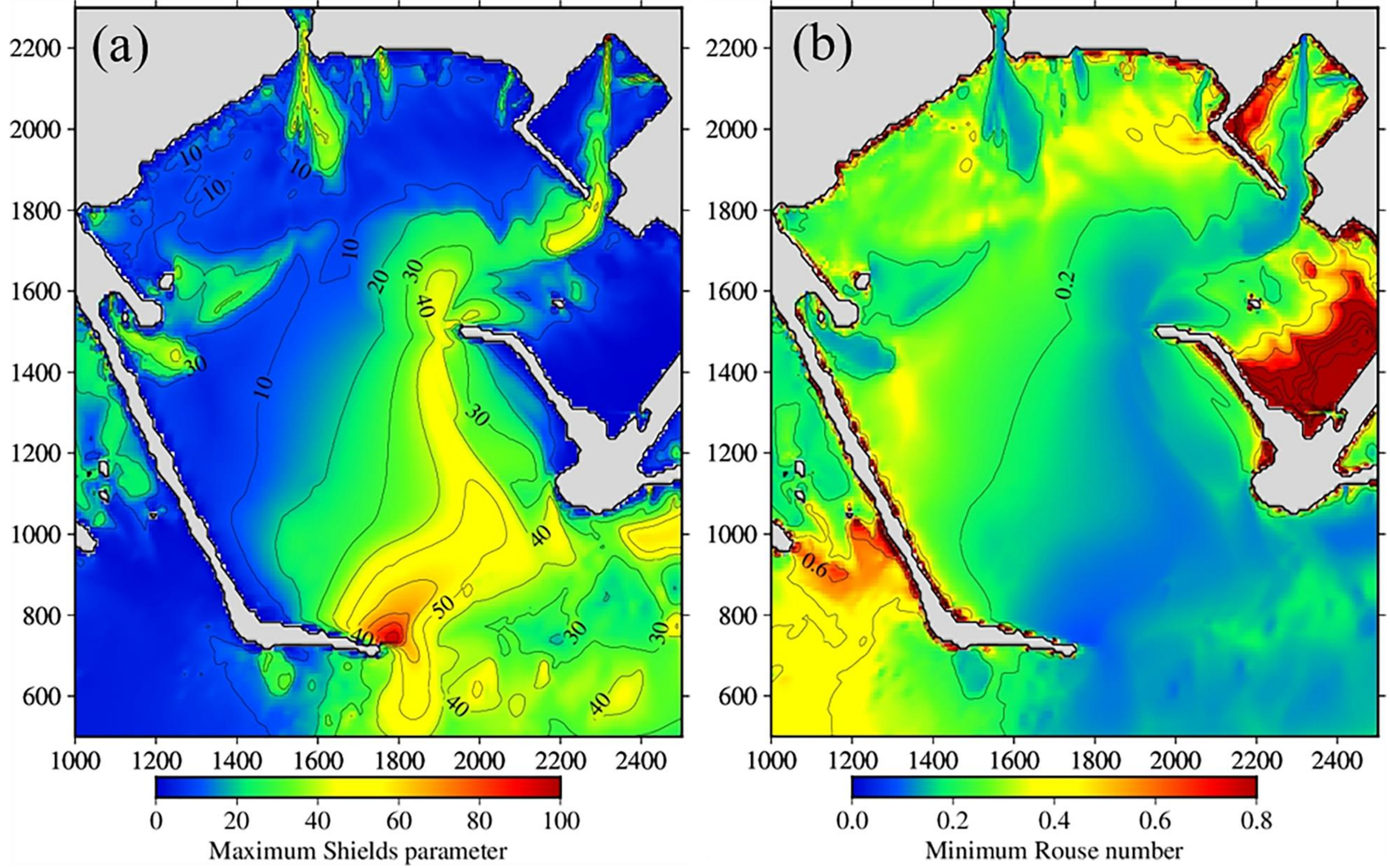

Fig. 14 Spatial distribution of sediment mobility from the 2011 Tohoku tsunami at Crescent City Harbor, USA . (a) Maximum Shields parameter. (b) Minimum Rouse number. Axis labels correspond to distance in meter within the level-5 grid.

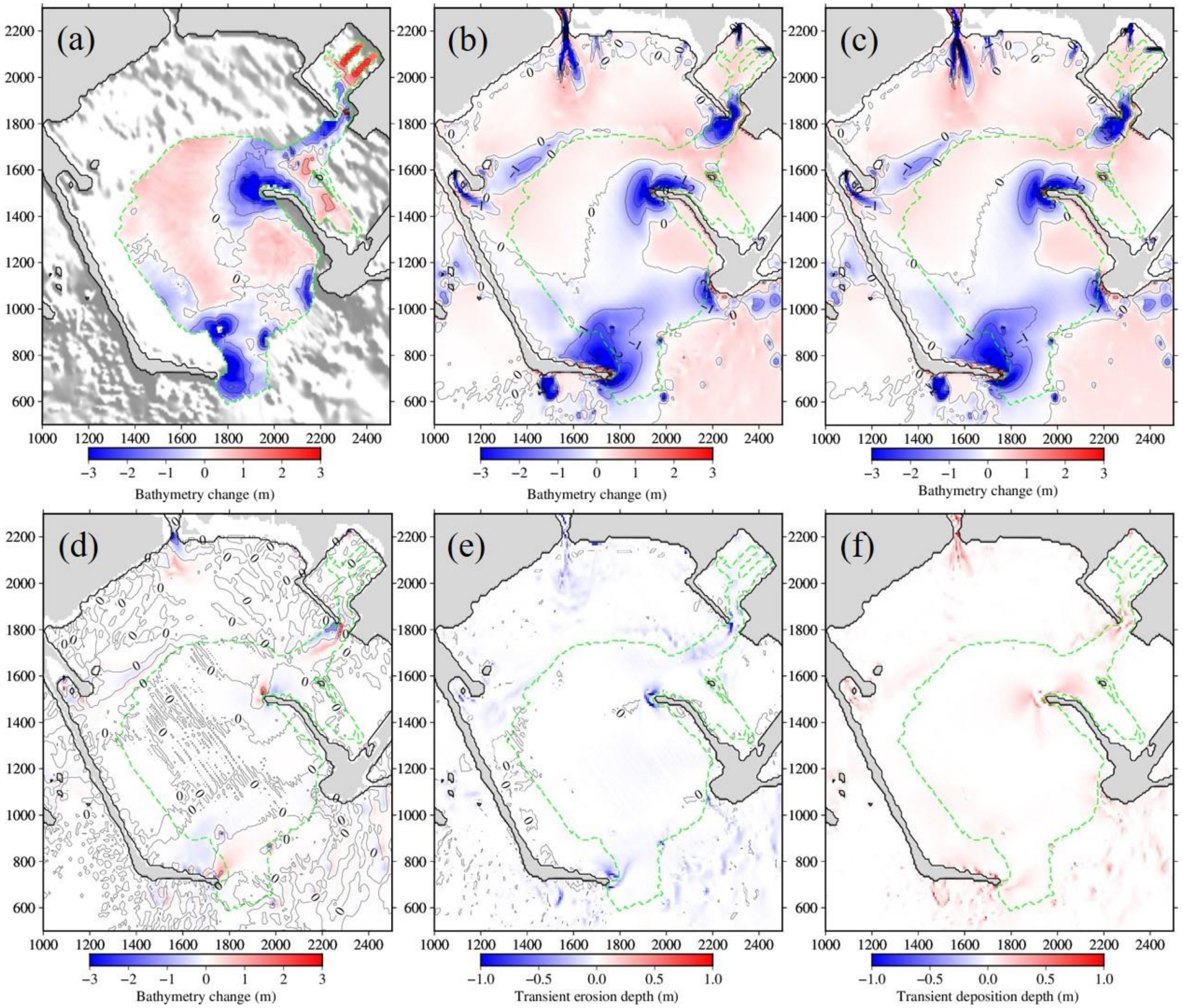

Fig. 15 Recorded and computed bathymetric changes from the 2011 Tohoku tsunami at Crescent City Harbor, USA. (a) Post-event survey from Wilson et al. (2012a). (b) Cumulative bathymetry change in full transport calculation with bed and suspended loads. (c) Cumulative bathymetry change in partial transport calculation with suspended load only. (d) Cumulative bathymetry change in partial transport calculation with bed load only. (e) Maximum transient erosion depth from bed load in full calculation. (f) Maximum transient deposition height from bed load in full calculation. Axis labels correspond to distance in meter within the level-5 grid and green dashed lines delineate the survey area.

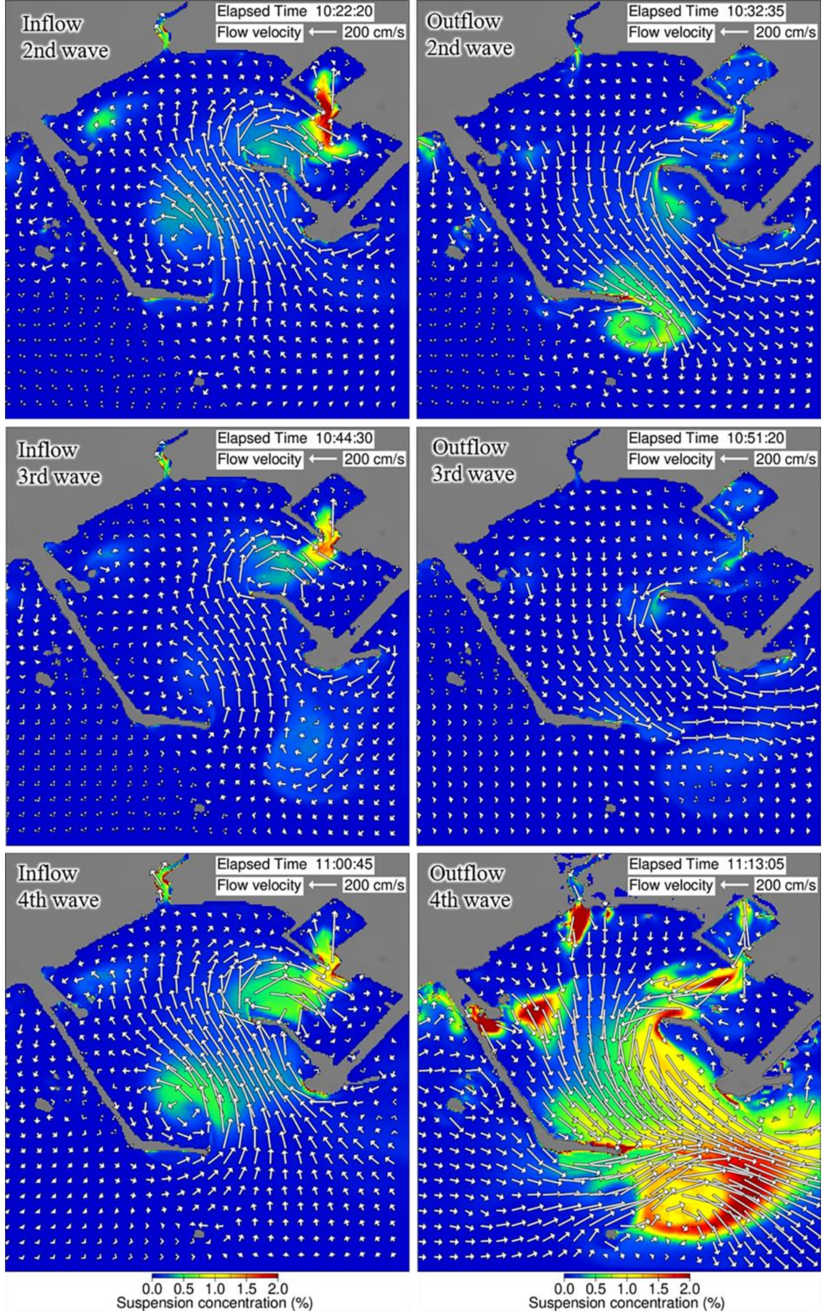

Fig. 16 Snapshots of flow velocity and sediment concentration at peak flow during the second, third, and fourth waves of the 2011 Tohoku tsunami at Crescent City Harbor, USA.